SHORT WAVELENGTH ELECTROSTATIC WAVES

IN THE EARTH'S MAGNETOSHEATH

by

Dennis L. Gallagher

An Abstract

Of a thesis submitted in partial fulfillment
of the requirements for the degree of
Doctor of Philosophy in Physics
in the Graduate College of
The University of Iowa

July, 1982

Thesis supervisor: Professor Donald A. Gurnett

ABSTRACT

Recent observations with the ISEE-1 spacecraft have found electric field emissions in the dayside magnetosheath whose frequency spectrum is modulated at twice the spacecraft spin period. The upper frequency cutoff in the frequency-time spectrum of the emissions has a characteristic parabola shape or "festoon" shape. The low frequency cutoff ranges from 100 Hz to 400 Hz, while the high frequency limit ranges from about 1 kHz to 4 kHz. The bandwidth is found to minimize for antenna orientations parallel to the wave number vectors, requiring the confinement of those vectors to a plane which contains the geocentric solar ecliptic coordinate z-axis. The spacecraft observed frequency spectrum results from the spacecraft antenna response to the Doppler shifted wave vector spectrum which exists in the plasma. Imposed constraints on the plasma rest-frame wave vectors and frequencies indicate that the emissions occur within the frequency range from about 150 Hz to 1 kHz, with wavelengths between about 30 meters and 600 meters. These constraints strongly suggest that the festoon-shaped emissions are ion-acoustic waves. The small group velocity and $\vec{k}$ direction of the ion-acoustic mode are consistent with wave generation upstream at

the bow shock and convection downstream to locations within the outer dayside magnetosheath.

Abstract approved: _Donald A. Gurnett_
                    Thesis supervisor

                    Professor, Physics and Astronomy
                    Title and department

                    July 21, 1982
                    Date

SHORT WAVELENGTH ELECTROSTATIC WAVES

IN THE EARTH'S MAGNETOSHEATH

by

Dennis L. Gallagher

A thesis submitted in partial fulfillment
of the requirements for the degree of
Doctor of Philosophy in Physics
in the Graduate College of
The University of Iowa

July, 1982

Thesis supervisor: Professor Donald A. Gurnett

Graduate College
The University of Iowa
Iowa City, Iowa

CERTIFICATE OF APPROVAL

————————————

PH.D. THESIS

————————————

This is to certify that the Ph.D. thesis of

Dennis L. Gallagher

has been approved by the Examining Committee
for the thesis requirement for the Doctor of
Philosophy degree in Physics at the July, 1982
graduation.

Thesis committee: _____
                       Thesis supervisor

_____
Member

_____
Member

_____
Member

_____
Member

ACKNOWLEDGMENTS

spacecraft. Lee Reinleitner has been willing to listen and critique my work as it progressed.

Some ideas or problems are just so dumb, that you wouldn't even tell your mother. That's why God made fellow graduate students. That process of mutual catharsis between graduate students is what makes us seem reasonable to everyone else. Thank you Lee, Mark, Bill, Dave, Bob, and Jim.

Although there is always a captain of the ship, who guides the destiny of all aboard, someone has to pull the oars. Thank you Kathy for typing this thesis and those papers, no matter how many changes; Bob and Tom for seeing that I didn't go hungry and probably knowing where all the money goes; John, Jeana, and Joyce for their professional drafting of figures, on time; Paul and Dora for the processing of wideband data that this work could not have been done without; Bob, Tom, and Bill just for making programs really work on the Univac computers; and Grace, who in the final analysis is the one that convinced the graduate college I was done.

ABSTRACT

Recent observations with the ISEE-1 spacecraft have found electric field emissions in the dayside magnetosheath whose frequency spectrum is modulated at twice the spacecraft spin period. The upper frequency cutoff in the frequency-time spectrum of the emissions has a characteristic parabola shape or "festoon" shape. The low frequency cutoff ranges from 100 Hz to 400 Hz, while the high frequency limit ranges from about 1 kHz to 4 kHz. The bandwidth is found to minimize for antenna orientations parallel to the wave number vectors, requiring the confinement of those vectors to a plane which contains the geocentric solar ecliptic coordinate z-axis. The spacecraft observed frequency spectrum results from the spacecraft antenna response to the Doppler shifted wave vector spectrum which exists in the plasma. Imposed constraints on the plasma rest-frame wave vectors and frequencies indicate that the emissions occur within the frequency range from about 150 Hz to 1 kHz, with wavelengths between about 30 meters and 600 meters. These constraints strongly suggest that the festoon-shaped emissions are ion-acoustic waves. The small group velocity and $\vec{k}$ direction of the ion-acoustic mode are consistent with wave generation upstream at the bow shock and convection downstream to locations within the outer dayside magnetosheath.

TABLE OF CONTENTS

LIST OF FIGURES

lower panel from 0 to 1 kHz. The 10 kHz channel

has a low frequency instrument cutoff at 650 Hz and

data below 150 Hz in the 1 kHz channel has been

eliminated in order to enhance the shading of the

higher frequencies. The emission extends to as

high as 5 kHz and shows a periodic gap in intensity

at all frequencies. A second frequency component

is evident at about 23 seconds, however, it may be

Figure 5   Wideband data from ISEE-1 is shown for November 22,

1977 (day 326) from 9h 59m 30s to 9h 59m 45s. The

spacecraft is located at about 12.3 R_E, 12.9° mag-

netic latitude, and 10.9 hours magnetic local time.

panels display kHz frequency-time spectrograms; the

upper panel from 0 to 10 kHz and the lower panel

from 0 to 1 kHz. The 10 kHz channel has a low fre-

quency instrument cutoff at 650 Hz and data below

150 Hz in the 1 kHz channel has been eliminated in

order to enhance the shading of the higher frequen-

cies. The frequency-time structure rises as high

as 6 kHz, showing gaps in intensity near 37 seconds

levels at labeled decibel values referenced to the
peak value. The model qualitatively reproduces the
emission festoon-shape and the intensity gap at all
frequencies for antenna orientations perpendicular
to the polarization electric field. The wave number
and electric field vectors are both at $\theta = 90°$ for
the purpose of illustrating the antenna response to

Figure 17   Antenna response intensity contours are compared
directly to an event observed with the wideband
receiver. Measurement of the antenna orientation to
the projected vector wave number determines horizon-
tal registration with the antenna response contours
and spectral shape is used to obtain vertical regis-
tration. The contour lines are found to reproduce
the festoon-shape spectrum and also reflect the shape
of the intensity gap at about 38.95 seconds. The
intensity dropout is about 5 degrees wide in space-
craft rotation at 1.3 kHz and widens to 15 degrees
at about 2 kHz. The match between model antenna
response and the festoon-shaped emission determines
a linear relationship between observed frequency and
magnitude of the spin-plane projected component of

and panels 1E through 7E are the corresponding

plots for electrons. Detectors 1 through 7 have

look-angles ranging from northward to southward-

looking, respectively, with detector 4 centered on

the ecliptic plane. Each panel displays energy and

sample time vertically and azimuthal spin angle

horizontally. Particle intensities are displayed

with color varying from deep blue for the minimum

particle fluxes and bright red for the largest (see

Frank et al., [1978] for further details). The

distributions for both electrons and ions are typi-

cal of near subsolar magnetosheath flows. Pre-

dominantly anti-sunward ion flow is evident as an

intensification near the center of the 5P and 6P

The ion-acoustic mode dispersion equation is

plotted against the allowed values of wave number

and frequency from Figure 18. Before resonance at

the ion plasma frequency, the dispersion curve

crosses allowed wave numbers from about 150 Hz to 1

kHz. For plasma flow relative to the spacecraft of

about 156 km/s and maximum wave number of 1.8×10^{-3} cm^{-1}, Doppler shifts as large as 4500 Hz are

I.   INTRODUCTION

Wideband electrostatic noise is a general description of all low frequency electrostatic waves which are characterized by a wide spectrum of frequencies. Waves of this nature are found to be associated with velocity shears in the auroral regions [Kintner, 1976], within the Earth's distant magnetosphere on auroral field lines [Gurnett and Frank, 1977], at boundary layers such as the plasma sheet boundary layer in the magnetotail [Gurnett et al., 1976], and the dayside magnetosheath [Anderson et al., 1982]. Most forms of broadband electrostatic waves appear to be associated with particles current or turbulent processes and few events are found to possess any discrete features in frequency-time spectrograms. Without discrete spectral features, it is difficult to associate the spectrum with a particular wave mode. Usually plasma wave emissions are identified with a discrete frequency such as the electron plasma frequency or found to possess a well-defined upper or lower frequency cutoff as in the case of continuum radiation [Gurnett and Shaw, 1973]. The waves which are studied in this thesis are electrostatic, broadband in frequency, and found within the outer magnetosheath. They are unique, however, in that they possess discrete spectral features. The observation of these waves was first published by Anderson et al. [1982]. Anderson described the appearance of these waves in 0-10 kHz frequency-time spectrograms to be like that of

"garlands hanging in a curve" or "festoon-shaped". The upper frequency cutoff in the frequency-time spectrum of the emissions has a characteristic parabola shape, analogous to a ribbon hanging in a curve. Figure 1 shows an example of the festoon-shaped emissions. This figure shows a frequency versus time spectrogram of electric fields from the ISEE-1 wideband receiver. The darker shaded regions correspond to higher electric field intensities. The characteristic rise and fall of the upper cutoff frequencies of the emission is the feature referred to as a festoon. As will be discussed, the festoon-shaped modulation of the upper cutoff frequency is directly related to the rotation of the spacecraft.

The purpose of this work is to examine the observed wave characteristics and to extend that information to a description of the wave environment and origins. First restrictions on the possible wave number-frequency spectrum of the waves in the plasma frame of reference are inferred by model-fitting the antenna response. Wave polarization can be determined when wave intensity is modulated in amplitude by the rotation of the dipole antenna used in the observation [Gurnett et al., 1976]. For an emission characterized by a single wavelength larger than the dipole antenna, the antenna response is sinusoidal with its rotation. When a spectrum of wave numbers ($k = 2\pi/\lambda$) is present with wavelengths both less than and greater than the antenna length, the antenna response is more complex. Next, cold plasma wave modes [Stix, 1962] and hot plasma wave modes [Krall and Trivelpiece, 1973] are examined as candidates for explaining the "festoon-shaped" wave emissions. Plasma wave modes are evaluated on the basis of satisfying the restrictions

imposed by antenna response modeling and the plasma environment of the spacecraft. Finally, the possible origins of these emissions are discussed. Wave generation at locations within the magnetosheath and at the bowshock are considered.

II. ANTENNAS AND INSTRUMENT DESCRIPTION

This study uses data acquired by the International Sun-Earth Explorer Satellites (ISEE) 1 and 2. These spacecraft are in highly ellipical orbits inclined at about 30 degrees to the ecliptic plane, with an apogee near 22.5 R_E. The plasma wave instruments on the mother-daughter pair are designed to provide high sensitivity measurements of plasma waves in the Earth's magnetosphere. The antennas and instruments that provide the data used in this study are described below.

The measurements from the ISEE-1 spacecraft which are used here are made with the 215 meter fine wire electric dipole antenna of the type shown in the upper portion of Figure 2. The antenna is normal to the spin axis of the spacecraft. The antenna rotates in a plane referred to as the spin plane which is essentially coplanar with the solar ecliptic plane. Magnetic field measurements are made with a triaxial search coil magnetic antenna. The antenna and spacecraft rotate with a 3-second period.

A high-time resolution spectrum analyzer and wideband receiver are used to measure the fluctuating fields observed with the ISEE-1 antenna. The spectrum analyzer consists of a 20-channel analyzer covering the frequency range from 5.62 Hz to 311 kHz and a 14-channel analyzer covering the frequency range from 5.62 Hz to 10 kHz. These analyzers provide relatively coarse frequency resolution with bandwidths of ± 15 percent

up to 10 kHz, and ± 7.5 percent for 10 kHz and above. The 20-channel analyzer is used here for electric field measurements and the 14-channel analyzer for magnetic field measurements. The data from the wideband receiver are obtained when the frequency bands from 10 Hz to 1 kHz and from 650 Hz to 10 kHz are available. These bands provide for much higher frequency and time resolution than the spectrum analyzer, however, absolute amplitudes are more difficult to obtain due to an automatic gain control, used in the wideband receiver.

ISEE-2 electric field measurements are made with the 30 meter fine wire electric dipole antenna shown in the bottom section of Figure 2. Magnetic field measurements are made with a single-axis search coil magnetic antenna identical to the search coil antenna used on ISEE-1. The spacecraft spins with a rotation period of 3 seconds. The antenna spin-plane of ISEE-2 is essentially the same as that of ISEE-1.

The ISEE-2 spacecraft also contains a high-time resolution spectrum analyzer and a wideband receiver. The spectrum analyzer has 16 frequency channels ranging from 5.62 Hz to 31.1 kHz. The bandwidths and center frequencies of these channels are identical to the spectrum analyzer on the ISEE-1 spacecraft. All channels of the spectrum analyzers on both spacecraft are sampled once per second in the low data rate mode and 4 times per second in the high data rate mode. The wideband receiver on ISEE-2 is similar to that on the ISEE-1 spacecraft. More detailed information about the plasma wave instruments on board the ISEE-1 and ISEE-2 spacecrafts can be found in Gurnett et al. [1978].

III. CHARACTERISTICS OF FESTOON-SHAPED EMISSIONS

A. Frequency Versus Time Characteristics

The basic characteristics of the festoon-shaped emissions are illustrated in Figures 3, 4, and 5. In each illustration, 15 seconds of data from the wideband instrument on ISEE-1 are shown. The bottom panel presents data from the 1 kHz bandwidth channel and the upper panel is from the 10 kHz bandwidth channel. One complete spacecraft rotation occurs from 9:57:06 UT to 9:57:09 UT in Figure 3. During this time the bandwidth of the wave spectrum appears to maximize at about 6, 7.5, and 9 seconds. The lower panel in Figure 3 more clearly shows the frequency structure below 1 kHz. At these frequencies, the main emission appears to fall and rise in frequency. For these times in Figure 3, the lower frequency cutoff of the emission band varies from 200 Hz to 600 Hz. The upper frequency cutoff of the emission band varies from about 700 Hz to 2 kHz. Figure 4 shows slightly different features. At approximately 20.5 seconds and 22.0 seconds, a dropout in intensity appears at all frequencies. It is around these times that the bandwidth is maximized. At the minima in the bandwidth of the main emission, a second distinct frequency component appears in the spectrum. The second frequency component, however, appears at sporadic times with respect to the main frequency-time structure. The frequency-time structure of the main emission is less clear in the 1 kHz channel in Figure 4, although

there is the suggestion of an asymmetry in the lower frequency compo-
nent of the waves. The band of emissions in this figure is seen to
extend as high as about 5 kHz and perhaps lower than 200 Hz. Figure 5
is similar to Figure 4 and shows the additional event times that are
examined in more detail below.

B. Frequency Spectra

Spectrum analyzer electric field measurements for a typical ISEE-1
pass through the magnetosphere are shown in Figure 6. The spectrum
analyzer channels are displayed vertically with frequency increasing
upward. Time is plotted horizontally, increasing to the right. The
spectral intensity in each channel is displayed logarithmically with a
dynamic range of 100db full scale. The bow shock encounter at about
0900 UT is characterized by a sharp increase in wave intensity in the
frequency channels from 17.8 Hz through 5.62 kHz. Festoon-shaped waves
are first seen after the bow shock encounter and the event chosen for
analysis extends from 0957 UT to 1000 UT. During this time, the spec-
tral power is seen to fall off rapidly with increasing frequency, up to
as high as perhaps 10 kHz.

Although a magnetic component exists at the chosen event times,
the frequency range is limited to the lowest channel at 5.6 Hz extend-
ing up to the 311 Hz channel. Magnetic field intensities fall to the
instrument noise level in the frequency range of the festoon-shape
electric field specturm. In a plasma, the ratio of magnetic field
strength to electric field strength in the relation cB/E gives the
local index of refraction (n) for electromagnetic waves if they are

propagating parallel to the magnetic field. The ratio can be used to test the electrostatic character of a wave. If $cB/E \ll n$, the wave may be considered to be electrostatic. The measured value of cB/E at about 600 Hz is 4.5. Because the magnetic field strength is at instrument noise level, the measured value of the ratio is equal to or greater than its true value. The index of refraction may be computed for whistler mode waves [Stix, 1962], for example, using the plasma density and field values from Appendix A and for the wave vector along the magnetic field. At a frequency of 600 Hz, the index of refraction is about 40. The measured value of cB/E is too small to be consistent with cold plasma whistler mode waves. Only under certain circumstances in a hot plasma will the index of refraction become small for an electromagnetic wave. When this happens, an electromagnetic wave will appear electrostatic. Consequently, these waves are thought to be effectively electrostatic.

C. Spectral Structure Versus Antenna Orientation

To fully understand the relationship between the antenna orientation and the observed spectral characteristics, it is first useful to review the characteristic directions that can exist in these observations. Only two directions are relevant to the analysis of these data: the local magnetic field direction and the plasma flow direction. These directions are summarized in Figure 7. The center drawing represents a three-dimensional sketch of the plasma flow velocity and magnetic field vectors, in geocentric solar ecliptic (GSE) coordinates. The sketch to the upper right shows these vectors projected into the

Y-Z plane, the sketch to the left shows the vectors projected into the X-Z plane, and the lower sketch shows the vectors projected into the X-Y plane (also the antenna spin plane). The orientation angles are given in the X-Y plane, because the electric dipole antenna measures potential differences only in the spin plane of the antenna. The plasma flow vector is obtained from the quadrispherical LEPEDEA instrument on ISEE-1 [Frank et al., 1978]. This vector is the result of a first moment calculation over the observed particle distribution in the proton energy range 215 eV to 45 keV. Although this calculation of velocity was made over an 8-minute interval of time, the preceding and following velocity calculations differ by no more than ±2% in magnitude and less than ±2° in direction. The average plasma flow velocity is therefore fairly constant. The magnetic field vector is obtained from the Russell experiment as presented in the ISEE A and B data pool tapes described in Ogilvie and Banks [1977], with no more than a ±4% change in magnitude and less than a ±10° change in direction for measurements on either side of the selected time. It also appears to be nearly constant. As can be seen in this sketch, the plasma flow is primarily anti-sunward. The direction and magnitude is consistent with the spacecraft location just inside the bow shock. The magnetic field is northward and in the dusk direction, consistent with the spacecraft location north of the ecliptic plane and at pre-noon local times.

The correspondence between spectral features in the wideband data and spacecraft antenna orientation is shown in Figures 8, 9, and 10. In the lower panels, antenna orientation is plotted with respect to the spacecraft-sun line (solid line), the spin-plane projected magnetic

field direction (short dashed line), and the projected plasma flow direction (long dashed line). In each figure, vertical reference lines are drawn showing the antenna direction when the emission bandwidth is maximized (time of symmetry in the periodic spectral structure). As can be seen, the antenna at the reference points is neither parallel nor perpendicular to the local magnetic field. Nor does the spectral structure appear simply related to the plasma flow direction. For the times marked by the vertical lines in Figures 8, 9, and 10, the antenna orientation to the plasma flow and magnetic field directions is summarized in Figure 11. For the group of points corresponding to each figure, the spread in angle is small. For the Figure 8 data, the magnetic field angle is 104 ± 3 degrees; for Figure 9 it is 121 ± 4 degrees and for Figure 10 it is 77 ± 4 degrees. Between these times, however, the orientation angle varies significantly. The orientation angle for those times when the bandwidth is a maximum was found to vary erratically between 0° and 90° over an 8-minute time interval, which included 242 festoon events. No systematic variation or relationship of the antenna orientation to the local magnetic field or plasma flow directions was found.

Upon reexamination of the wideband data, such as found in Figures 3, 4, and 5, it is apparent that the specific spectral shape under study is not seen continuously. It occurs for 6 to 10 seconds at a time, separated either by intervals of spectrally diffuse wideband noise or a momentary loss of the characteristic spectral shape. It seems that each period during which the festoon-shaped emissions occur is a separate and perhaps localized event. Given the measured plasma

flow of about 160 km/s, the events are localized in regions that are from 760 km to 1600 km in spatial size. This sporadic occurrence of festoon-shaped emissions was also reported by Anderson et al. [1982], where the occurrence was correlated to low frequency magneto-acoustic waves. Tsurutani et al. [1982] has most recently identified those low frequency-long wavelength magnetohydrodynamic structures as non-oscillatory "waves" generated by the drift mirror instability. The festoon-shaped emissions were observed during the high magnetic field and low density phase of these magnetohydrodynamic structures.

D. Observation Locations

Detailed locational surveys of the festoon-shaped electric field events are difficult because of the very short time scale of this type of spectral features. Normal electric field surveys of ISEE-1 and -2 observations are routinely performed with the spectrum analyzer showing 24 hours of data at a time. Routine surveys are also performed with the wideband receiver data. This processing of the wideband data shows frequency-time structure with one minute time resolution. Even on this scale, the festoon-shaped features cannot be uniquely identified. Firm identification of the festoon-shaped modulation requires the time con-suming process of spectrum analyzing wideband data at real-time rates. The events which have been found begin at the bow shock and extend inward to locations which approach the magnetopause, i.e., within the outer magnetosheath. Events are found on the dayside of the Earth, from 6 hours to 18 hours magnetic local time. It will be shown that the frequency-time character of these emissions is a consequence of the

polarization of the observed waves and the antenna pattern for varying wavelengths. Because the festoon shape of the emission is a consequence of the dipole antenna and emission polarization and not magnetosheath location, a single interval of observations will be studied in detail and used to develop an understanding of the observed frequency-time structure.

The ISEE-1 spacecraft trajectory, during the event which will be studied, is shown in Figures 12 and 13. The event occurs from about 0900 UT to 1000 UT on November 22, 1977 (day 326). Figure 12 shows a noon-midnight projection of the ISEE-1 orbit. The event occurs just inside the bow shock at a latitude in geocentric solar magnetospheric (GSM) coordinates of about 12 degrees. Figure 13 shows an equatorial projection of the spacecraft orbit. The spacecraft is on an inbound trajectory at about 11 hours magnetic local time.

IV. ANTENNA RESPONSE

The previous sections discussed the observational characteristics of the festoon-shaped spectrograms. The relationship of the festoon-shape feature to the rotation of the spacecraft is strong evidence that the spacecraft antenna is influencing the detection of the broadband electric field emissions in the magnetosheath. Before the emission spectrum can be examined, it is first necessary to derive an expression giving the antenna response to a wave in the plasma. This derivation is done in the following sections. When the antenna response is known, it will be used with the observed spectrum to deduce constraints on the true emission spectrum.

A. Antenna Response Derivation

From Maxwell's equations, the electric field in a system is given by

$$\vec{E} = -\nabla\phi - \frac{1}{c}\frac{\partial \vec{A}}{\partial t} \tag{1}$$

Because the observed waves have no magnetic component so that $\frac{\partial \vec{A}}{\partial t} = 0$, the above expression reduces to

$$\vec{E} = -\nabla\phi \quad . \tag{2}$$

This relation can be re-expressed as an integral along the line element $\vec{ds}$

$$\phi = -\int \vec{E} \cdot \vec{ds} \tag{3}$$

The potential difference between two points can be found by performing the integration along the line between the points. The wave is assumed to be a plane wave, where the vector components are in general complex.

$$\vec{E} = (E_x \hat{x} + E_y \hat{y} + E_z \hat{z}) e^{i(\vec{k} \cdot \vec{r} - \omega t)} \tag{4}$$

For electrostatic waves, the time origin can be chosen such that the electric field vector components are purely real. Also, the electric field and wave number vectors are parallel. The integral over a distance $\vec{\ell}$ along the antenna then takes the form

$$\phi(\ell, t) = -\int_{-\vec{\ell}/2}^{\vec{\ell}/2} (E_x \hat{x} + E_y \hat{y} + E_z \hat{z}) \cdot (\cos \theta \hat{x} dx + \sin \theta \hat{y} dy) e^{i(\vec{k} \cdot \vec{r} - \omega t)} \tag{5}$$

where θ is the orientation angle of the antenna (see Figure 14 for a sketch of the vector orientations and angle definitions). In cylindrical coordinates, after taking the dot product, using

$$\hat{x} = \hat{\rho} \cos \theta - \hat{\theta} \sin \theta,$$

$$\hat{y} = \hat{\rho} \sin \theta + \hat{\theta} \cos \theta,$$

$$\hat{z} = \hat{z}, \quad \text{where}$$

$\hat{\rho}$ and $\hat{\theta}$ are unit vectors in cylindrical coordinates.

Equation 5 then becomes

$$\phi(\ell,t) = - \int_{-\ell/2}^{\ell/2} [(E_x \cos \theta + E_y \sin \theta)d\rho \; e^{i(\vec{k}\cdot\vec{\rho} - \omega t)} \tag{6}$$

where for an arbitrary vector $\vec{A}(x,y,z) = A_x \hat{x} + A_y \hat{y} + A_z \hat{z}$, we have used

$$\vec{A}(\rho,\theta,z) = (A_x \cos \theta + A_y \sin \theta)\hat{\rho} + (A_y \cos \theta - A_x \sin \theta)\hat{\theta} + A_z \hat{z}$$

After integration, Equation 6 becomes:

$$\phi(\ell,t) = -2(\vec{E}\cdot\hat{\ell}) \frac{\sin(k'_\rho \frac{\ell}{2})}{k'_\rho} e^{-i\omega t} \quad , \tag{7a}$$

where $\hat{\ell}$ is a unit vector along the antenna,

$$\vec{E}\cdot\hat{\ell} = E_x \cos \theta + E_y \sin \theta, \quad \text{and}$$

$$k_\rho' = k_x \cos\theta + k_y \sin\theta, \tag{7b}$$

is the component of the $\vec{k}$ vector along the antenna axis. The sin x/x
term in Equation 7a is the standard radio interferometer pattern
[Kraus, 1966]. Equation 7a can be simplified somewhat by noting that

$$k_x = k_\rho \cos\alpha_k , \qquad k_y = k_\rho \sin\alpha_k , \qquad \text{and}$$

$$k_\rho' = k_\rho[\cos\alpha_k \cos\theta + \sin\alpha_k \sin\theta] = k_\rho \cos(\alpha_k - \theta)$$

where k_ρ is the magnitude of the component of the wave vector in
the antenna spin plane and α_k is the azimuthal angle of the wave
vector from the x-axis as shown in Figure 14. The potential measured by
the plasma wave instrument will be proportional to the average potential
applied across that length of the spacecraft antenna which actively
responds to the potential in the plasma. For the moment, assume that
the observed potential is the average potential across the antenna
lengths from L_1 to L_2. Assuming perfect coupling, the observed
potential is given by the following integral:

$$\overline{\phi(t)} = \int_{L_1}^{L_2} \phi(\ell,t)\,d\ell \Big/ \int_{L_1}^{L_2} d\ell \tag{8}$$

Now include the expression for $\phi(\ell, t)$.

$$\overline{\phi(t)} = \frac{-2}{L_2 - L_1} \int_{L1}^{L_2} (\vec{E} \cdot \hat{\ell}) \frac{\sin(k'_\rho \frac{\ell}{2})}{k'_\rho} e^{-i\omega t} d\ell \quad . \tag{9}$$

Since only the sine term is a function of ℓ, the integral becomes:

$$\overline{\phi(t)} = \frac{-2}{L_2 - L_1} (\frac{\vec{E} \cdot \hat{\ell}}{k'_\rho}) e^{-i\omega t} \int_{L_1}^{L_2} \sin(k'_\rho \frac{\ell}{2}) d\ell \quad . \tag{10}$$

After evaluating the integral and applying the trigonometric identity $\cos(\alpha) = 1 - 2\sin^2(\alpha/2)$, the observed potential is expressed as the following:

$$\overline{\phi(t)} = \frac{4}{(L_2 - L_1)} (\vec{E} \cdot \hat{\ell}) (\frac{\sin^2(\frac{k'_\rho L_1}{4}) - \sin^2(\frac{k'_\rho L_2}{4})}{k'^2_\rho}) e^{-i\omega t} \quad . \tag{11}$$

The power spectrum (P) observed by the spacecraft is proportional to the square of the measured antenna potential ($\overline{\phi}$), where the antenna potential is purely real for electrostatic waves. The final expression is obtained by time averaging P(t) over the wave period.

$$P \propto [(\vec{E} \cdot \hat{\ell}) (\frac{\sin^2(\frac{k'_\rho L_1}{4}) - \sin^2(\frac{k'_\rho L_2}{4})}{k'^2_\rho (L_2 - L_1)})]^2 \tag{12}$$

$k'_\rho \propto \omega$

$\frac{k'_\rho L_1}{4} = 0$

B. Antenna Coupling to Plasma

Two terms are evident in the above expression. The first term involving $\vec{E}\cdot\hat{\ell}$ is a function of the wave polarization as it projects into the antenna spin plane. This term provides the usual sinusoidal modulation of observed wave intensity as the electric dipole antenna rotates. The second term involving $\sin^2(\frac{k'_\rho L}{4})$ is a function of the wave number magnitude and direction and the active lengths of the spacecraft antenna. As illustrated in Figure 2, the ISEE-1 antenna has a tip-to-tip length of 215 meters, of which 143 meters is covered with an insulator. The value of L_2 is 215 meters for ISEE-1 and 30 meters for ISEE-2. For ISEE-2, $L_1 \approx 1$ meter, corresponding to the diameter of the spacecraft body. For ISEE-1, the value of L_1 depends upon whether the antenna responds resistively or capacitively to the applied signal. If the antenna responds resistively, only the uninsulated 36 meters at the ends of the dipole elements contribute to the measured potential. If the antenna responds capacitively, then the entire antenna length contributes to the measured potential. Figure 15 displays the relative amplitude of the second term in Equation 13 as a function of $k_\rho L_2/4$ for $L_1 = 1$ meter and $L_1 = 143$ meters. The value of $k_\rho L_2/4$ is varied from 0 to 3π where $\theta = \alpha_k$. As expected, the log-log plots show a characteristic $\sin x/x$ variation with x. For $L_1 = 1$ meter, the amplitude has a power law dependence with wave number, giving a slope of -4. For $L_1 = 143$ meters, however, the amplitude falls off faster than a power law dependence.

To determine the appropriate value of L_1, the critical frequency separating the resistive and capacitive antenna coupling domains must be estimated. Aggson and Kapetanakos [1966] examine the source impedance of a wire antenna as it relates to antenna capacitance. The critical frequency for ISEE-1, in the magnetosheath, will be estimated by computing the ratios of the capacitive and resistive impedances between the Aggson and Kapetanakos study and the present study. In Aggson and Kapetanakos' study a wide range of magnetospheric altitudes were considered. The resistive source impedance (R_S) for a positively charged antenna (due to photo-ionization) is primarily dependent upon particle density and cross-sectional antenna area. Differences in R_S due to density will be removed by choosing an altitude in the Aggson and Kapetanakos study which corresponds to magnetosheath densities. The antenna treated by Aggson and Kapetanakos had a diameter of 1 cm and length of 100 cm. The uninsulated portions of the ISEE-1 antenna have a combined length of 7200 cm and diameter of about 0.1 cm. In Aggson and Kapetanakos' study, the source resistance is very roughly inversely proportional to cross-sectional area. The particle density from Appendix A can be used to select an altitude of 8 R_E, at which the antenna capacitance is computed by Aggson and Kapetanakos to be about 9 $\times$ 10^{-12} farads. Aggson and Kapetanakos computed capacity from the expression

$$C = \frac{2\pi\varepsilon_o d}{\ln\left(\dfrac{a + \lambda + \sigma\lambda_D}{a}\right)} \tag{13}$$

where
d = antenna length,

ε_o = 8.85 × 10^{-12} farad/m (permitivity constant),

a = antenna diameter,

λ = photo-ionization sheath thickness,

σ = 1, and

λ_D = Debye length.

The photo-ionization sheath thickness λ is computed from the expression

$$\phi_o = \frac{n_e e}{2\varepsilon_o} [(a + \lambda)^2 \ln \frac{a + \lambda + \sigma\lambda_D}{a} - \frac{1}{2}[(a + \lambda + \sigma\lambda_D)^2]]$$

where
ϕ_o is the antenna potential and

n_e is the particle density.

If the approximation a ≪ λ ~ λ_D is used, the expression for the sheath thickness λ becomes

$$\frac{2\varepsilon_o \phi_o}{n_e e} = \lambda^2 \ln \frac{\lambda + \lambda_D}{a} - \frac{1}{2}(\lambda + \lambda_D)^2$$

or

$$\frac{\lambda + \lambda_D}{a} = e^{(\frac{1}{2}(1 + \frac{\lambda_D}{\lambda})^2 + \frac{2\varepsilon_o \phi_o}{n_e e})}$$

Assuming an antenna potential on the order of $\phi_0 = 1$ volt, the value for λ is found to be about 194 cm, for the particle density in Appendix A. Using Equation 13 and this value for λ, the ISEE-1 antenna capacitance is estimated to be $C \sim 10^{-9}$ farads. The critical frequency is computed based on the following proportionality

$$f_o \propto \frac{1}{R_s C}$$

The ratio of the Aggson and Kapetanakos 8 R_E magnetospheric resistive source impedance to the ISEE-1 resistive source impedance will be on the order of the ratio of the cross-sectional antenna areas or 1/7.2. The ratio of the capacitances is on the order of 0.009. The critical frequency for ISEE-1 in the magnetosheath will be a factor of 1.25×10^3 less than that for Aggson and Kapetanakos' antenna at the magnetospheric altitude of 8 R_E ($\sim 2.7 \times 10^3$ Hz). The critical frequency is estimated to be on the order of 3 Hz. The festoon-shaped modulation occurs well above this frequency, and is therefore in the capacitive domain of antenna coupling. It will be assumed that the antenna couples capacitively to the plasma, so that the full length of the dipole elements actively respond to the applied plasma potential ($L_1 = 1$ meter). The left graph in Figure 15, therefore, describes the ISEE-1 antenna response to a spectrum of wave numbers.

C. Model Characteristics

Equation 12 defines the power spectrum of a fine-wire electric dipole antenna's response to a spectrum of wave numbers, as the antenna rotates. Besides antenna length, the antenna response depends primarily upon the angle between the electric field and the wave vectors projected into the spin plane. The antenna response is illustrated in Figure 16. In this figure, logarithmic, equal-intensity contours are drawn at -5 db, -10 db, -20 db, and -30 db. The vertical axis in the figure is normalized wave number $(k_\rho L_2/4)$ and the horizontal axis is antenna rotation angle (θ) in a coordinate system where both the wave vector and polarization electric field vectors are chosen to be at $\theta = 90$ degrees. The normalized wave number is chosen to range from 0 to 3π radians. The basis for choosing this parameter range is that the wave number-angle structure shown in Figure 16 qualitatively reproduces the frequency-time spectral structure of the festoon-shaped emissions, like that shown in Figure 1. For ISEE-2, the quantity $k_\rho L_2/4$ varies only from 0 to 1.315, for the same variation in k_ρ as plotted for ISEE-1. This means that the festoon-shaped effect will not be seen by the shorter ISEE-2 antenna for the values of k_ρ defined in Figure 16. For the selected event times, the density from Appendix A is approximately 58 cm^{-3} and the electron temperature is about 30 eV. This gives a Debye length (λ_{De}) on the order of 5 meters. An order of magnitude measure of the smallest wavelengths which can exist in a plasma is given by $k\lambda_{De} = 1$. The corresponding minimum wavelength is on the order of 34 meters. Because the antenna pattern effect seen in Figure 16 depends upon the existence of wavelengths less than the antenna length of 30 meters, the festoon-

shaped effect is not likely to be found with the ISEE-2 antenna, because the wavelengths are too long. What is found with ISEE-2 is a sporadic wideband structure extending from about 600 Hz to 3 kHz. No festoon-shaped modulation is found in the ISEE-2 wideband spectrograms.

Based on the above antenna modeling, the existence of wavelengths both shorter and longer than the antenna is sufficient to explain the structure in the frequency-time spectra illustrated in Figures 8, 9 and 10. The connection between wave number and frequency is described by the Doppler-shift equation

$$f' = f + \frac{\vec{k} \cdot \vec{V}}{2\pi} \tag{14}$$

where f and $\vec{k}$ are the plasma rest frame frequency and vector wave respectively, $\vec{V}$ is the relative motion of the plasma with respect to the spacecraft, and f' is the spacecraft observed frequency. The spacecraft velocity $\sim$ 2 km/s is much less than the plasma flow velocity, so it will not be included in $\vec{V}$. It will be shown later that festoons consist of wavelengths as small as about 36 meters. For plasma flow velocities on the order of 160 km/s, the Doppler shift term may then be as high as 4 kHz. It is clearly possible for a wave of essentially zero frequency ($f = 0$) in the plasma rest frame to be Doppler shifted into the observed frequency spectrum. For long wavelengths or small wave numbers, only the polarization term in Equation 12 is important. The usual cosine squared variation of intensity with antenna rotation is obtained under

this condition. As the wavelength becomes small (of the order of the dipole antenna length and less), the antenna orientation to the wave number direction becomes important. The minima in intensity resulting from the antenna model, satisfy the following relation:

$$m\pi = k_{\rho m}\cos(\alpha_k - \theta)L_2/4 \qquad (15)$$

From this equation, where m is an integer, it is clear that as the antenna angle (θ) becomes perpendicular to $\vec{k}$ (or specifically $\alpha_k - \theta \to \pm\pi/2$), larger values of $k_{\rho m}$ are required to satisfy the minima condition.

$$k_{\rho m} = \frac{4\pi m}{L_2 \cos(\alpha_k - \theta)}$$

The dependence of $k_{\rho m}$ on the antenna rotation angle is the reason for the festoon-shape seen in frequency-time spectra, because the first null in the frequency spectrum is proportional to $k_{\rho m}$. This result is similar to the measured power spectrum dependence on wave number and antenna orientation, derived for double-probes by Temerin [1979].

D. Detailed Model Evaluation of Selected Events

The next step is too apply the model described in Figure 16 to a specific event. The objective is to use the antenna response model as a

tool for determining the wave mode of the broadband electrostatic emissions. The event selected is on November 22, 1977 (day 326). The event occurs at a time when changes that effect the frequency-time structure, as observed with the wideband receiver, are minimized. The only parameter that must be determined is the orientation angle of the vector wave number as projected into the antenna spin plane. Figure 10 shows antenna orientations as a function of time and can be used to determine the parameter needed. The vertical time marks at about 37.5 and 39 seconds correspond approximately to the times when the antenna is perpendicular to the wave vector direction, or in this case about 154 degrees and 334 degrees (to the spacecraft-sun line), respectively. By matching the model to these angles and adjusting the vertical registration so as to match the frequency-time shape (in Figure 10) to wave vector-rotation angle contours (in Figure 16), the antenna response can be adjusted to fit the data. The results of this fitting procedure are shown in Figure 17. Given the limited dynamic range (at best 20db) of the wideband processing film, the antenna response model provides a very good fit to the observed spectrum. In Figure 18, the left vertical axis is the normalized wave number (just as in Figure 16), the bottom horizontal axis is the event time, the right vertical axis is the frequency scale corresponding to the wideband data displayed, and the top horizontal axis is the antenna orientation angle to the spacecraft-sun line for both the model and data during this event. The close correspondence between the shape of the model contours and the edge of the visible wideband frequency-time structure is clearly evident in Figure 17. At about 38.95 seconds the sharp "bite-out" at all frequencies corresponds

to the point where $\vec{E}\cdot\hat{\ell}$ goes to zero in the antenna response function (see Equation 12). The spectrum at other times follows the model's U-shaped or festoon-shaped appearance. That the bite-out is so sharply defined provides strong evidence that the direction of the projected wave vector distribution must be confined to a line in the antenna spin plane. The bite-out constrains the direction of the projected wave vector (k_ρ) to two possible orientations. The possible orientation angles are 64 degrees and 244 degrees. Were this not the case, a smearing in time and rotation angle in relationship to the antenna response model would be seen. It is estimated that the wave vector directions must be within ±5 degrees of the above values, otherwise substantial smearing would be observed.

A consequence of fitting the antenna model to the spectrum Figure 17 is that the frequencies observed in the spacecraft frame of reference are directly and linearly related to emission wave number component k_ρ. The range of normalized wave number from 0 to 3π

$$0 \leq \frac{k_\rho L_2}{4} \leq 3\pi \tag{16}$$

translates into a range of k_ρ magnitudes given in the following inequality:

$$0 \leq k_\rho \leq 1.75 \times 10^{-3} \text{ cm}^{-1} \tag{17}$$

where L_2 = 215 meters. Because the 10 kHz wideband channel used in Figure 17 has a lower cut-off frequency of 650 Hz and because the 1 kHz

channel does not provide clear spectral information, a minimum corresponding normalized wave number of 0.853 radians will be used. The ranges of frequency and wave number included in the model fit to wide-band data is expressed in the following inequalities:

$$650 \text{ Hz} \leq f' \leq 2490 \text{ Hz}$$
$$1.59 \times 10^{-4} \text{ cm}^{-1} \leq k_\rho \leq 1.75 \times 10^{-3} \text{ cm}^{-1} \tag{18}$$

where frequency (f') and wave number (k_ρ) are linearly related by the antenna model fit to the data. It must be noted that the limits defined in Equation 18 do not represent the limits of the observed spectrum, they simply represent corresponding limits for f' and k_ρ. These limits define the range of wave numbers and frequencies to which the antenna response model has been applied. The range of the wave number magnitude given in Equation 17 also translates into a range of wavelengths in terms of the Debye length given in the previous section.

$$7\lambda_{De} \leq \lambda \leq 74\lambda_{De}$$

The observed frequency and total wave number ($\vec{k}$, $|\vec{k}|^2 = k_\rho^2 + k_z^2$) are also related by the Doppler-shift given by Equation 14, where k_z is the z-component of the wave vector.

Because nothing is specifically known about the magnitude of k_z, the limits in Equation 18 provide constraints in wave number-frequency space for the waves observed. The allowed regions of wave-number and

frequency are obtained by varying k_z from negative infinity to positive infinity, for the two allowed orientation angles of k_ρ, to compute the corresponding values of frequency (f). This is done by expressing the Doppler shift equation as a function of f.

$$f = f' - \frac{1}{2\pi}(k_\rho(V_x\cos \alpha_k + V_y\sin \alpha_k) + k_zV_z) \tag{19}$$

The linear relation between observed frequency (f') and wave number (k_ρ) can be expressed as

$$f' = ak_\rho + b \tag{20}$$

where the fit in Figure 17 gives $a=1.16 \times 10^6$ cm.s^{-1} and $b=466$ Hz. Using the expression for f' in Equation 20 in Equation 19, the following expression is obtained:

$$f = \frac{(a - V_x\cos \alpha_k + V_y\sin \alpha_k)k_\rho}{2\pi} + b - \frac{V_zk_z}{2\pi} \tag{21}$$

For the two possible values of α_k (64 degrees and 244 degrees), for k_z varying from $-\infty$ to $+\infty$ at fixed values of k_ρ, and for selected values of k_ρ at 1.59×10^{-4} cm^{-1}, 3.5×10^{-4} cm^{-1}, 7.8×10^{-4} cm^{-1}, and 1.74×10^{-3} cm^{-1}, curves of allowed wave number-frequency values are shown in Figure 18. Two curves are obtained for each value of k_ρ. The curve corresponding to $\alpha_k = 64°$ minimizes higher in frequency than the other curve and exists for both positive and negative k_z. Solutions do not

exist for $\alpha_k=244$ degrees and $k_z>0$. These four families of curves are representative of a spectrum of possible wave number-frequency values for k_ρ varying smoothly over the range defined in Equation 17. The shaded region in Figure 18 defines those values which are allowed. Those values are approximately limited at large wave number by $k\lambda_{De} \leq 1$ ($T_e \approx$ 30 eV). The more lightly shaded regions define values allowed by only one of the two possible k_ρ orientations. The more heavily shaded region defines wave number and frequency values allowed with either orientation of k_ρ. The curve defining equal phase ($V_p = \omega/k$) and electron thermal velocities (V_{Te}) is also included in the illustration. Because cold plasma theory is only valid for $V_{Te}/V_p \ll 1$, warm or hot plasma theory will be necessary for describing the observed emissions.

V. IDENTIFICATION OF PLASMA WAVE MODES

The previous section developed an antenna response model which lead
to constraints on the possible values of wave number and frequency for a
particular event. It is the objective of this section to examine the
commonly known plasma wave modes as they relate to the plasma environ-
ment in order to try to identify the wave modes involved in producing
the festoon-shaped features. Those wave modes which may contribute
to the emissions are determined by means of this examination. Appendix
A lists measured and computed plasma parameters which will be useful in
the following analysis.

A. Cold Plasma Modes

Although Figure 19 indicates that cold plasma descriptions are not
valid, at least for electron wave modes, cold plasma formalism provides
useful descriptions of most of the wave modes found in hot plasma
theories. The treatment of Stix [1962] will be followed for a review of
cold plasma wave theory. The notation, definitions of terms, and
general dispersion equation can be found in Appendix B.

Beginning at the lowest frequencies are the hydromagnetic wave
modes or Alfven waves. The most significant approximation in deriving
the expression for the Alfven modes is $|\omega| \ll \omega_{ci}$. The dispersion rela-
tions from Equations 21 and 22 of Stix [1962] are

$$\omega^2 = \frac{(k_x^2 + k_z^2)c^2}{1 + \frac{4\pi\rho c^2}{B_o^2}} \qquad \text{and} \qquad (22)$$

$$\omega^2 = \frac{k_z^2 c^2}{1 + \frac{4\pi\rho c^2}{B_o^2}} . \qquad (23)$$

Equation 22 describes the ordinary or fast hydromagnetic mode and Equation 23, the extraordinary or slow-mode. The corresponding dispersion curves are shown in Figure 20 for frequencies below 10^{-2} Hz. The shaded regions shown in this illustration represent the track of the solutions of the cold plasma dispersion equation of Appendix B as the angle of the vector wave number to the magnetic field is varied from 0 degrees to 90 degrees. That region corresponding to the slow-mode Alfven wave is shown for angles only to 75 degrees. This mode disappears as $\theta \rightarrow 90$ degrees. For those angles near zero degrees, both Alfven wave modes are electromagnetic. They become quasi-electrostatic when both of the following inequalities are satisifed.

$$|\omega| \ll \omega_{ci}$$

$$\omega_{ci}^2 \sin^4\theta \gg 4\omega^2 \cos^2\theta \qquad (24)$$

It is clear from these conditions for quasi-electrostatic Alfven waves and the dispersion curves in Figure 20, that the corresponding wave numbers are too small to contribute to the festoon-shaped electrostatic emissions.

The slow-mode Alfven wave becomes the ion cyclotron wave as $\omega \to \omega_{ci}$. For a two component plasma there is a resonance at the ion cyclotron frequency for $\theta = 0$ degrees and moves to lower frequencies as θ becomes larger. The mode disappears as $\theta \to 90$ degrees, just as the slow-mode Alfven modes disappear. Although the resonant dispersion curve intersects the region of wave number-frequency space required for festoon-shaped emissions, ion cyclotron waves are highly damped for wavelengths much less than the ion gyroradius. From the magnetic field strength in Appendix A and an ion temperature of about 90 eV (see Figure 1 of Sckopke et al. [1981], the ion gyroradius is about 40 km. The festoon-shaped events have wavelengths much less than this, therefore, ion cyclotron waves can be excluded from further consideration.

The fast-mode Alfven wave dispersion relation is unaffected by the ion cyclotron frequency, but encounters a resonance which moves from the electron cyclotron frequency to the lower hybrid resonance as θ varies from 0 degrees to 90 degrees, respectively. The sense of polarization reverses for this wave as it crosses the lower hybrid resonance frequency. The wave modes which have resonance angles between the electron cyclotron frequency and lower hybrid resonance are called whistler mode waves. There is also a resonance at the upper hybrid frequency. This latter resonance, however, is not apparent in Figure 20 due to the proximity of a cutoff for this mode (at $L = 0$) to resonance at the

electron plasma frequency. Both of these modes are also electromagnetic, except at resonance where the modes become quasi-electrostatic. Although resonance at the upper hybrid frequency may reach large wave numbers, this mode is too high in frequency to account for the festoon-shaped spectrograms. Above the electron plasma frequency, the quasi-longitudinal wave mode is electromagnetic and also too high in frequency to account for the festoon-shaped spectrograms.

Whistler mode resonances remain a possible source of the festoon-shaped events. Additional constraints on whistler mode waves may be derived, because of the characteristics of a wave mode at a resonance. Before proceeding, it is desirable to sketch the geometry in the antenna spin-plane, as is done in Figure 20. The projected plasma flow and magnetic field vectors are shown along with the orientation of k_ρ. Because k_ρ is confined to a line in the antenna spin-plane and k_z is essentially unknown, there exists a plane within which the vector wave number must be contained. For this special case, that plane can be projected into a line in the spin-plane. Additional restrictions can be made by realizing that resonance of a whistler wave mode at a particular angle to the magnetic field is a source of large wave numbers. A wave vector directed along a resonance cone could produce the required wave number spectrum, but would be characterized by vector wave numbers confined to a narrow range of angles to the magnetic field. By defining the resonance cone angle (α_{kB}), it becomes possible to solve for k_z from the following equation

$$\vec{k} \cdot \vec{B} = kB \cos \alpha_{kB} = k_\rho (B_x \cos \alpha_k + B_y \sin \alpha_k) + k_z B_z \qquad (25)$$

where $k = \sqrt{k_\rho^2 + k_z^2}$

Equation 25 is quadratic in k_z and for each of the two possible values of α_k, two values of k_z can be computed. The roots of Equation 25 are plotted in Figure 21. As might be expected, the roots are double valued along the two curves which are plotted. Naturally, the values of the solutions for k_z or equivalently for $|\vec{k}|$ depend upon the value of k_ρ. Equation 18 defines the range of k_ρ which is known to exist. If the maximum value for k_ρ from Equation 18 is used, the largest $|\vec{k}|$ which would be known to exist for a given resonance cone angle could be found. It is for these values that the curves in Figure 21 are plotted. This means that a given resonance cone angle requires the existence of wave numbers at least as large as those defined by the curves in Figure 21. The wave number corresponding to $k\lambda_{De} = 1$ is marked in Figure 21, for a minimum electron temperature of 30 eV [Sckopke et al., 1981; Thorne and Tsurutani, 1981; private communication, M. F. Thomsen [1982]. Krall and Trivelpiece [1973] determined that for a maxwellian particle velocity distribution, whistler mode waves are weakly Landau damped except for $\lambda \lesssim a_{ce}$, where

$$a_{ce}^2 = \frac{kT_e}{m_e \omega_{ce}^2} = \lambda_{De}^2 \frac{\omega_{pe}^2}{\omega_{ce}^2}$$

From the parameters in Appendix A, the condition for strong damping becomes $\lambda \lesssim 100 \lambda_{De}$. Because whistler mode waves will be strongly damped for the wave numbers known to exist, it is unlikely that the whistler mode is responsible for the festoon-shaped events.

The remaining cold plasma wave modes occur at high frequencies just above the electron plasma frequency. These are quasi-transverse "ordinary" and "extraordinary" waves. They exhibit a cutoff at and just above the electron plasma frequency. Both waves are electromagnetic and can be discarded as candidates for explaining the magnetosheath electrostatic emissions.

B. Hot Plasma Modes

There are several electrostatic wave modes which are unique to hot plasma theory. The first to be considered are the solutions of the Harris dispersion equation at $\theta = \pi/2$, called Bernstein modes. Bernstein modes are solutions to the Harris dispersion relation at frequencies between either the ion or the electron cyclotron harmonics. For $\omega_{pe}/\omega_{ce} \sim 1$, Bernstein modes exhibit resonances at cyclotron harmonics. As $\omega_{pe}/\omega_{ce} \gg 1$, solutions to the dispersion equation may couple across gyroharmonic frequencies. Appendix A gives the ratio of ω_{pe}/ω_{ce} at the event time that has been studied as ≈ 100. For such high values of the ratio, resonances no longer appear at cyclotron harmonics (see Tataronis and Crawford [1970] for "ring" particle distribution function). The behavior of the dispersion curves becomes highly dependent upon the particle distribution function. However, the condition for the instability of Bernstein mode waves is that $\partial f_0/\partial v_\perp > 0$ for

some range of $v_\perp > 0$ [Tantaronis and Crawford, 1970]. Measurements of the electron and proton particle distribution functions at energies from 215 eV to 45 keV by the quadrispherical LEPEDEA on board ISEE-1 are shown in Figure 22, for the event time which has been chosen for study. In the illustration, there are two sets of panels; panel 1P through 7P for ions and 1E through 7E for electrons. Each group of panels corresponds to detector look-angles ranging from northward to southward-looking, respectively, with the 4P and 4E detectors centered on the ecliptic plane. Each panel displays energy and sample time vertically and azimuthal spin angle horizontally. Particle intensities are displayed with a color-coded scale ranging from deep blue for minimum intensities to bright red for the maximum (see Frank et al. [1978] for further details). The distributions for both electrons and ions are characteristic of near subsolar magnetosheath flows. Because there is no positive slope evident in the energy distributions in Figure 22, there is no positive slope in the particle velocity distribution functions. A significant temperature anisotropy ($T_\perp \neq T_\parallel$) is known to be a common feature of such magnetosheath distributions (see Thorne and Tsurutani [1981]). In that study, a temperature anisotropy was found to be associated with the magnetic field waves of the same slow-mode magneto-acoustic wave that Anderson et al. [1982] correlated with the observation of festoon-shaped emissions. The consequence of these particle observations is that there is no apparent source for the growth of Bernstein mode waves at energies above 215 eV. This also applies to the Harris mode waves corresponding to wave numbers at oblique angles to the magnetic field. That no positive slope in the plasma particle

distribution function is found is not conclusive evidence that it does not exist. A positive slope to the distribution function may exist at lower energies, however, it is likely that such a distribution is not a common feature of the magnetosheath [T. E. Eastman, private communication, 1982]. For the ion and electron temperatures stated in the previous section, the electron and proton gyroradii are 540m and 40km, respectively. Because these gyroradii are the characteristic length scales of the Bernstein modes and because the wavelengths of the festoon-shaped events are much less than these gyroradii, it is unlikely that the Bernstein modes are associated with the festoon-shaped events.

Besides low frequency-long wavelength particle drift or gradient wave modes, the only wave mode remaining to be considered is the ion acoustic mode. For the conditions $\omega_{ci} \ll \omega_{pi}$ and $\omega \gg \omega_{ci}$, which are valid in the regime being considered, descriptions of the ion-acoustic mode may be approximated by the case for zero magnetic field. Krall and Trivelpiece [1973] derive a dispersion equation for ion acoustic waves from linearized Vlasov theory of plasma waves in the free field case and using a Maxwellian distribution function.

$$\omega_{REAL}^2 = \frac{k^2 C_s^2}{1 + k^2 \lambda_{De}^2} \tag{26}$$

These waves are called sound waves because for $k\lambda_{De} \ll 1$ all wavelengths propagate at the ion sound speed C_s. For a maxwellian velocity distribution, the only condition given for the weak damping of these waves is

that $\omega_{IMAGINARY} \ll \omega_{REAL}$ or equivalently $T_e \gg T_i$. Stated another way, the ion and electron thermal velocities must be related to the phase velocity as shown in the following inequality:

$$(\frac{kT_i}{m})^{1/2} < \frac{\omega}{k} < (\frac{kT_e}{m_e})^{1/2} \tag{27}$$

Equation 26 is plotted in Figure 23, against the region of antenna model constrained wave number and frequency. The dispersion curve intersects the shaded region from about 150 Hz to 1 kHz. Ion-acoustic mode wave emission within this frequency range will satisfy observationally imposed constraints. Note that this does not require wave emission at all frequencies within the range, only some frequencies within the range. For a plasma flow of 156 km/s (from Appendix A) and for a maximum wave number of about 1.8×10^{-3} cm^{-1} (from Figure 23), Doppler shifts may be as large as $kV/2\pi = 4500$ Hz (from Equation 14). Depending upon the angle between the wave number and plasma flow velocity, the observed emission spectrum can be produced. Figure 23 also appears to resolve the ambiguity in the orientation of k_ρ. For $\alpha_k = 244°$, the full rest-frame spectrum limits marked in Figure 23 are allowed. The spectrum for $\alpha_k = 64°$ is limited to frequencies no less than about 500 Hz. Also, if $k\lambda_{De} = 1$ is used to roughly indicate the level of Landau damping, then damping will be less for $\alpha_k = 244°$ than for $\alpha_k = 64°$. The addition of a magnetic field into a description of the ion-acoustic mode can also result in the resonant frequency rising at about $\sqrt{1.6}\omega_{pi}$ [Stix, 1962]. For such a situation, higher values of k_ρ may be reached

without increasing the total wave number. The orientation of k_ρ for α_k = 244° will still result in less damping than for α_k = 64°. It is therefore, more likely that the vector wave numbers are aligned with α_k = 244°. This orientation is generally downstream of the bow shock in the direction of the bulk plasma flow.

VI. DISCUSSION

Emissions likely to be ion-acoustic mode waves have been found up-stream of the bow shock (foreshock) in the solar wind [Anderson et al., 1981]. Although no festoon-shaped effect was reported, Figure 15 of Anderson et al. [1981] shows evidence of a rising and falling emission band with periods on the order of half the spacecraft rotation period. It is possible that this is also an antenna pattern effect. Outward flowing particles apparently reflected at the bow shock and associated with ion-acoustic mode waves in the Earth's foreshock are also observed [Eastman et al., 1981]. Most recently, unstable electron particle distributions have been found just inside the Earth's bow shock [Feldman et al., 1982]. The distributions are characterized by a convecting Maxwellian superimposed on a Lorentzian distribution. This particle distribution is found to be a common characteristic of the plasma just inside the bow shock. The distribution is believed to be unstable in the frequency range from 100 Hz to 1.5 ω_{pi} to ion-acoustic waves [private communication, M. F. Thomsen, 1982], although correlations with wave observations have not yet been done.

The generation of ion-acoustic mode waves could occur at locations within the outer magnetosheath or at a surface such as the bow shock. It has been stated that the festoon-shaped spectrograms, which probably result from ion-acoustic mode waves, are seen at widely ranging loca-

tions in the outer magnetosheath, and at the bow shock. That the emissions are a common occurrence is support for bow shock generation. Generation of the emissions at this surface is supported because particle distributions unstable to ion-acoustic waves have not been commonly found within the magnetosheath [T. E. Eastman, private communication, 1982]. Particle distributions which may be unstable to the ion-acoustic mode have been found at the bow shock [Feldman et al., 1982]. Examination of the ion-acoustic mode group velocities for the frequency range of interest finds the magnitudes to be less than the plasma flow velocity. Group velocity ($V_g = \partial\omega/\partial k$) as a function of frequency is plotted in Figure 24. From about 150 Hz to 1 kHz the ion-acoustic mode group velocity is at least a factor of 3 less than the plasma flow velocity, so these waves will be carried by the bulk plasma flow. If the nominal magnetosheath plasma is not unstable to ion-acoustic waves, the emissions must originate in association with the bow shock and be convected to spacecraft locations within the outer magnetosheath. Because festoon-shaped events are not found within the inner magnetosheath, generation at the magnetopause or in the magnetosphere is not likely.

Further evidence for bow shock generation of the festoon-shaped events comes from the observed wave vector geometry. Wave vectors are found to lie within a plane which contains the GSE z-axis and vary in orientation to the GSE x-axis with time. There is no apparent local reason for the wave vector to be confined to a plane. The required geometry can be found upstream at the bow shock. Should wave vectors be produced at orientations defined by the bow shock surface, that

orientation might be preserved as the wave is convected downstream. Variation in the local orientation of the plane containing the wave vector would then reflect a time history of the variation of the surface of the bow shock immediately upstream of the spacecraft. A systematic drop in the intensity of the festoon-shaped events with distance from the bow shock (into the magnetosheath) provides additional confirming evidence. The variation in intensity as a function of the distance from the bow shock can be seen in Figure 6 for those frequency channels covering the ion-acoustic wave spectrum. These logarithmically displayed intensities are a maximum just inside the bow shock and decline in intensity until the festoon-shaped events disappear near 1000 UT. At 600 Hz, the spectral power flux decreases at a rate of about 3db per 100 km for the first 2000 km after the bow shock and remains fairly constant until about 1000 UT. This effect is consistent with waves which are produced at the bow shock and dissipate as they are convected away from the source of free energy driving the instability.

A concern associated with the propagation of ion-acoustic waves from the bow shock to spacecraft locations within the magnetosheath is that ion-acoustic waves are strongly damped unless $T_e/T_i \ll 1$. Thorne and Tsurutani [1981] state that magnetosheath protons have thermal energies considerably larger than electrons ($T_i \approx 200$ eV). In general, the ion to electron temperature ratio in the magnetosheath is found to be $3 \leq T_i/T_e \leq 10$ [Ogilvie and Scudder, 1979; Sckopke et al., 1981; T. E. Eastman, private communication, 1982]. For the specific event studied, and the measured plasma flow and wave group velocities, the transit time of ion-acoustic waves from bow shock to the spacecraft is

no less than about 30 seconds. If the ion-acoustic waves were heavily damped by the magnetosheath plasma, they would not be observed at the spacecraft location. As discussed above, some damping is evident as the spacecraft becomes further from the bow shock. However, detailed growth rate calculations with observed particle distributions are necessary, before it can be determined if bow shock wave generation is consistent with these observations. Of interest is the appearance of two levels of damping in Figure 6. The effect may reflect the thermalization of solar wind ions entering the magnetosheath. Electrons experience an abrupt change in thermal temperature at the bow shock, while ions thermalize more slowly [M. F. Thomsen, private communication, 1982]. Because the damping of ion-acoustic waves will be strongly influenced by T_e/T_i, the sharp drop in intensity of the waves during the first 2000 km after crossing the bow shock and passing into the magnetosheath may correspond to the region over which solar wind ions thermalize in the magnetosheath and at the bow shock.

VII.   CONCLUSIONS

This study has sought to explore the characteristics and causes of the "festoon-shaped" electric field spectrum found in the Earth's magnetosheath.   The importance of understanding these emissions is evident by their frequent occurrence.   They are seen over wide ranges of local time and across the outer magnetosheath.   The "festoon-shape" seen in frequency-time spectrograms results from the dipole antenna pattern for electric field wavelengths longer than ($\lambda \sim 600$ meters) and shorter than ($\lambda \sim 30$ meters) the ISEE-1 antenna ($L = 215$ meters).   Given the Doppler shift of a plasma frame spectrum of wave vectors, the observed frequency is shown to be linearly related to the wave number component in the antenna spin-plane.   The fine time structure evident in the spectral shape is a consequence of the confinement of all wave number vectors to a plane which contains the z-axis in GSE coordinates and projects to a line in the antenna spin plane.

Of all the cold and hot plasma wave modes considered, the restrictions which are imposed upon possible wave number-frequency values in the plasma frame of reference eliminate likely participation of all but one normal plasma wave mode in the generation of these emissions.   That mode is the ion-acoustic wave mode.

In the rest frame of the plasma, the ion-acoustic waves are produced at frequencies in the range from about 150 Hz to 4 kHz and at

wavelengths from about 30 meters to 600 meters. The ion-acoustic waves are thought to be produced upstream at the Earth's bow shock, where electrons passing through a shock acceleration region produce an unstable particle velocity distribution. It is additionally hypothesized that the wave vectors are produced with orientations defined by the bow shock surface and that this geometry is characteristic of the waves as they are convected into the magnetosheath. The festoon-shaped events and, therefore, ion-acoustic waves are found to be a common characteristic of the Earth's dayside magnetosheath.

A self-consistent picture has been assembled of the magnetosheath environment during the observation of electrostatic fields which exhibit a "festoon-shaped" frequency-time structure in phase with the rotation of the observing dipole antenna. This does not mean that these observations may have no other explanation. It does mean that any explanation of all salient features is highly constrained by the collection of presented evidence. Should this picture be sustained by subsequent investigation, an additional tool is obtained for the study of the complex processes operating in the Earth's magnetosheath and at the bow shock.

REFERENCES

Aggson, T.L., and C.A. Kapetanakos, On the impedance of a satellite borne VLF electric field antenna, NASA, X-612-66-380, 1966.

Anderson, R.R., C.C. Harvey, M.M. Hoppe, B.T. Tsurutani, T.E. Eastman, and J. Etcheto, Plasma waves near the magnetopause, J. Geophys. Res., 87, 2087-2107, 1982.

Anderson, R.R., G.K. Parks, T.E. Eastman, D.A. Gurnett, and L.A. Frank, Plasma waves associated with energetic particles streaming into the solar wind from the Earth's bow shock, J. Geophys. Res., 86, 4493-4510, 1981.

Eastman, T.E., R.R. Anderson, L.A. Frank, and G.K. Parks, Upstream particles observed in the Earth's foreshock region, J. Geophys. Res., 86, 4379-4395, 1981.

Feldman, W.C., R.C. Anderson, S.J. Bame, S.P. Gary, J.T. Gosling, D.J. McComas, M.F. Thomsen, G. Paschmann, and M.M. Hoppe, Electron velocity distributions near the Earth's bow shock, submitted for publication to J. Geophys. Res., 1982.

Frank, L.A., K.L. Ackerson, R.J. DeCoster, and B.G. Burek, Three-dimensional plasma measurements within the Earth's magnetosphere, Space Sci. Rev., 22, 739-763, 1978.

Frank, L.A., D.M. Yeager, H.D. Owens, K.L. Ackerson, and M.R. English, Quadrispherical LEPEDEAS for ISEE-1 and -2 plasma measurements, IEEE Trans. Geosci. Electr., GE-16, 3, 221-224, 1978.

Gurnett, Donald A., and Robert R. Shaw, Electromagnetic Radiation trapped in the magnetosphere above the plasma frequency, J. Geophys. Res., 78, 8136-8149, 1973.

Gurnett, D.A. and L.A. Frank, and R.P. Lepping, Plasma waves in the distant magnetotail, J. Geophys. Res., 81, 6059-6071, 1976.

Gurnett, D.A. and L.A. Frank, A region of intense plasma wave turbulence on auroral field lines, J. Geophys. Res., 82, 1031-1050, 1977.

Gurnett, D.A., F.L. Scarf, R.W. Fredricks, and E.J. Smith, The ISEE-1 and ISEE-2 plasma wave investigation, IEEE Trans. Geosci. Electr., GE-16, 3, 225-230, 1978.

Kintner, P.M. Jr., Observations of velocity shear driven plasma turbulence, J. Geophys. Res., 81, 5114-5122, 1976.

Krall, Nicholas A., and Alvin W. Trivelpiece, Principles of Plasma Physics, McGraw-Hill, 1973.

Kraus, John D., Radio Astronomy, McGraw-Hill, 1966.

Ogilvie, K.W. and M.D. Banks, Jr., Notes on the ISEE A+B data pool tape, NASA/Goddard Space Flight Center, X-692-77-129, 1977.

Ogilvie, K.W., and J.D. Scudder, First results from the 6-axis electron spectrometer on ISEE-1, Space Sci. Rev., 23, 123-133, 1979.

Sckopke, N., G. Paschmann, G. Haerendel, B.U.O. Sonnerup, S.J. Bame, T.G. Forbes, E.W. Hones, and C.T. Russell, Structure of the low-latitude boundary layer, J. Geophys. Res., 86, 1981.

Stix, Thomas Howard, The Theory of Plasma Waves, McGraw-Hill, 1962.

Tantaronis, J.A., and F.W. Crawford, Cyclotron harmonic wave propagation and instabilities, I. Perpendicular propagation, J. Plasma Phys., 4, 231-248, 1970.

Temerin, Michael, Dopler shift effects on double-probe-measured electric field power spectra, J. Geophys. Res., 84, 5929-5934, 1979.

Thorne, R.M., and B.T. Tsurutani, The generation mechanism for magnetosheath lion roars, Nature, 293, 384-386, 1981.

Tsurutani, B.T., E.J. Smith, R.R. Anderson, K. W. Ogilvie, J.D. Scudder, D.N. Baker, and S.J. Bame, Lion roars and non-oscillatory drift mirror waves in the magnetosphere, submitted to J. Geophys. Res., 1982.

APPENDIX A:

MEASURED AND COMPUTED PLASMA PARAMETERS

Basic Plasma and Wave Environments

density $n = n_e \approx n_i = 58$ cm^{-3}

    [Bame experiment, Ogilvie and Banks, 1977; verified with plasma
    wave data]

magnetic field $|\vec{B}_0| = 24.4$ nT, $B_{ox} = 5.91$ nT, $B_{oy} = 20.4$ nT,
    $B_{oz} = 11.9$ nT
    [Russell experiment, Ogilvie and Banks, 1977]

kinetic electron temperature $T_e \approx 30$ eV
    [Tsurutani, 1982]

plasma flow velocity $|\vec{V}| = 156$ km/s, $V_x = -113$ km/s, $V_g = -74$ km/s,
    $V_z = 78$ km/s
    [T. E. Eastman, private communication, 1982]

thermal electron energy density $U_T = nkT = 2.8 \times 10^{-9}$ erg/cm^3

maximum average electric field energy density $U_E = \dfrac{E^2}{8\pi} = 4.9 \times 10^{-22}$
    erg/cm^3

Computed Plasma Parameters and Frequencies

Thermal/magnetic energy ratio	$\beta = 1.2$
Thermal electron velocity	$V_{Te} = 2.3 \times 10^8$ cm/s
Electron Debye length	$\lambda_{De} = 530$ cm
Ion sound speed	$C_S = 5.4 \times 10^6$ cm/s
Electron plasma frequency	$f_{pe} = 68$ kHz $\equiv \omega_{pe}/2\pi$
Electron gyrofrequency	$f_{ce} = 680$ Hz $\equiv \omega_{ce}/2\pi$
Ion plasma frequency	$f_{pi} = 1.6$ kHz $\equiv \omega_{pi}/2\pi$
Ion gyrofrequency (H^+)	$f_{ci} = 0.37$ Hz $\equiv \omega_{ci}/2\pi$
Upper hybrid resonance	$f_{UHR} = 68$ kHz $\equiv \omega_{UHR}/2\pi$
Lower hybrid resonance	$f_{LHR} = 16$ Hz $\equiv \omega_{LHR}/2\pi$
Electron plasma to gyrofrequency ratio	$\omega_{pe}/\omega_{ce} = 100$

APPENDIX B:

COLD PLASMA THEORY SUMMARY AND DEFINITIONS

General Cold Plasma Dispersion Equation

[Stix, 1962]

$$An^4 - Bn^2 + C = 0$$

where

$$A = S \sin^2\theta + P \cos^2\theta$$

$$B = RL \sin^2\theta + PS(1 + \cos^2\theta)$$

$$C = PRL$$

and where for a two-component plasma

$$R \equiv 1 - \frac{\omega_{pe}^2}{\omega^2}\left(\frac{\omega}{\omega - \omega_{ce}}\right) - \frac{\omega_{pi}^2}{\omega^2}\left(\frac{\omega}{\omega + \omega_{ci}}\right)$$

$$L \equiv 1 - \frac{\omega_{pe}^2}{\omega^2}\left(\frac{\omega}{\omega + \omega_{ce}}\right) - \frac{\omega_{pi}^2}{\omega^2}\left(\frac{\omega}{\omega - \omega_{ci}}\right)$$

$$P \equiv 1 - \frac{\omega_{pe}^2}{\omega^2} - \frac{\omega_{pi}^2}{\omega^2}$$

$$\overset{+}{n} = \frac{\overset{+}{k}c}{\omega}$$

Solution for Cold Plasma Dispersion Equation

$$n^2 = \frac{B \pm F}{2A}$$

where

$$F^2 = (RL - PS)^2 \sin^4\theta + 4P^2D^2\cos^2\theta$$

APPENDIX C:

FIGURES

Figure 1   Wideband data from the ISEE-1 spacecraft on

December 20, 1977 (day 354) illustrate the charac-

teristic festoon-shaped emissions found in the

Earth's dayside magnetosheath. The spacecraft is

located at about 18.6 R_E, 13.1° magnetic latitude

and 7.45 hours magnetic local time. The lower panel

shows an electric field spectrogram for the fre-

quency range of 0 to 5 kHz and for times from 18h

42m 28s to 18h 42m 54s universal time (higher inten-

sities are shown as darker shading). The upper

panel shows the trace of the upper frequency cut-

off of the emission as a function of time. The

rise and fall of the cutoff is directly related to

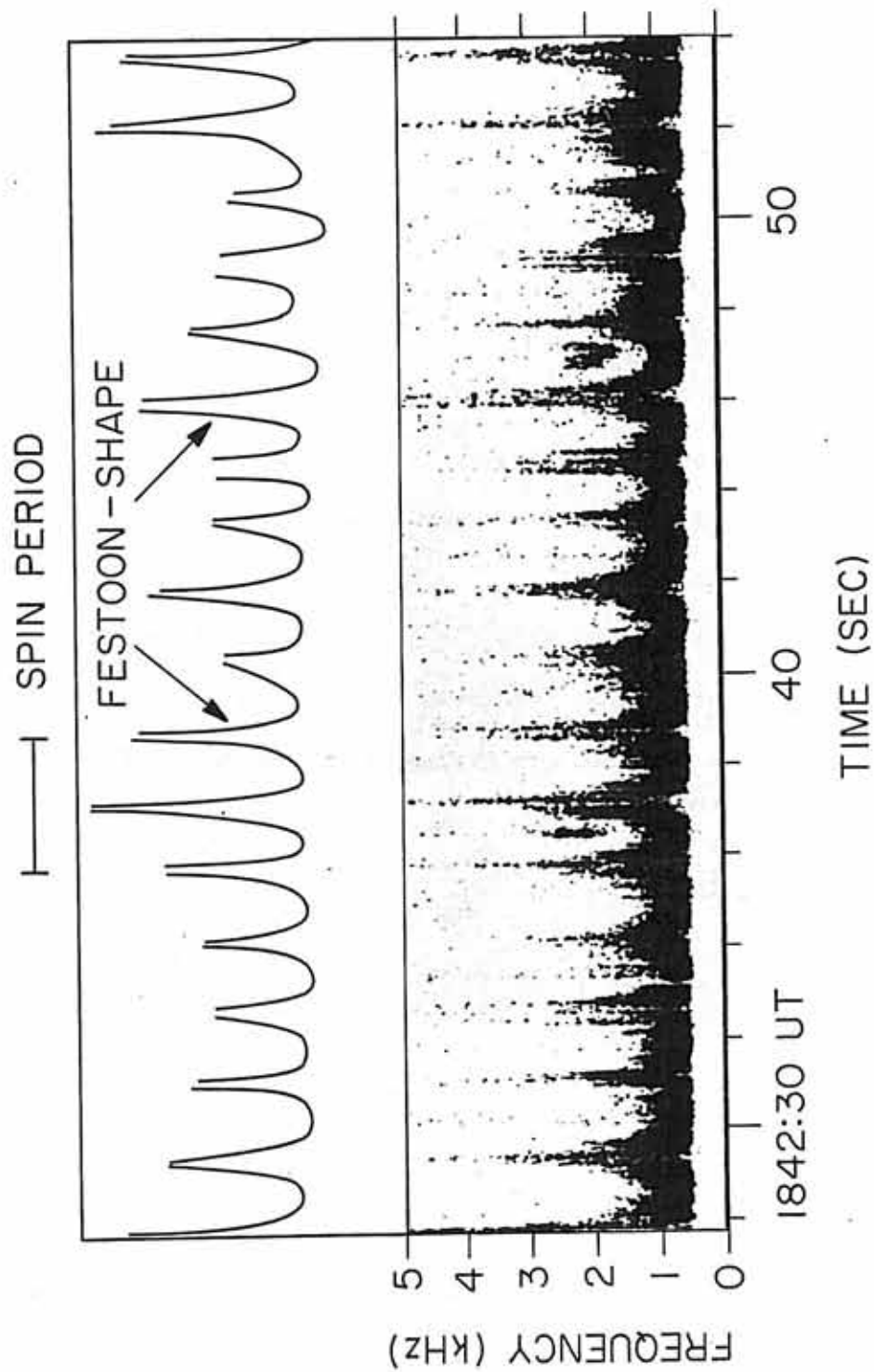the rotation of the spacecraft's dipole antenna.

FIGURE 1

Figure 2   The ISEE-1 and -2 long fine-wire electric dipole antennas are shown. They correspond to the V-axis and X-axis, respectively. The ISEE-1 antenna is 215 meters long tip-to-tip with 143 meters insulated and 36 meters exposed at each end. The ISEE-2 antenna is 30 meters tip-to-tip.
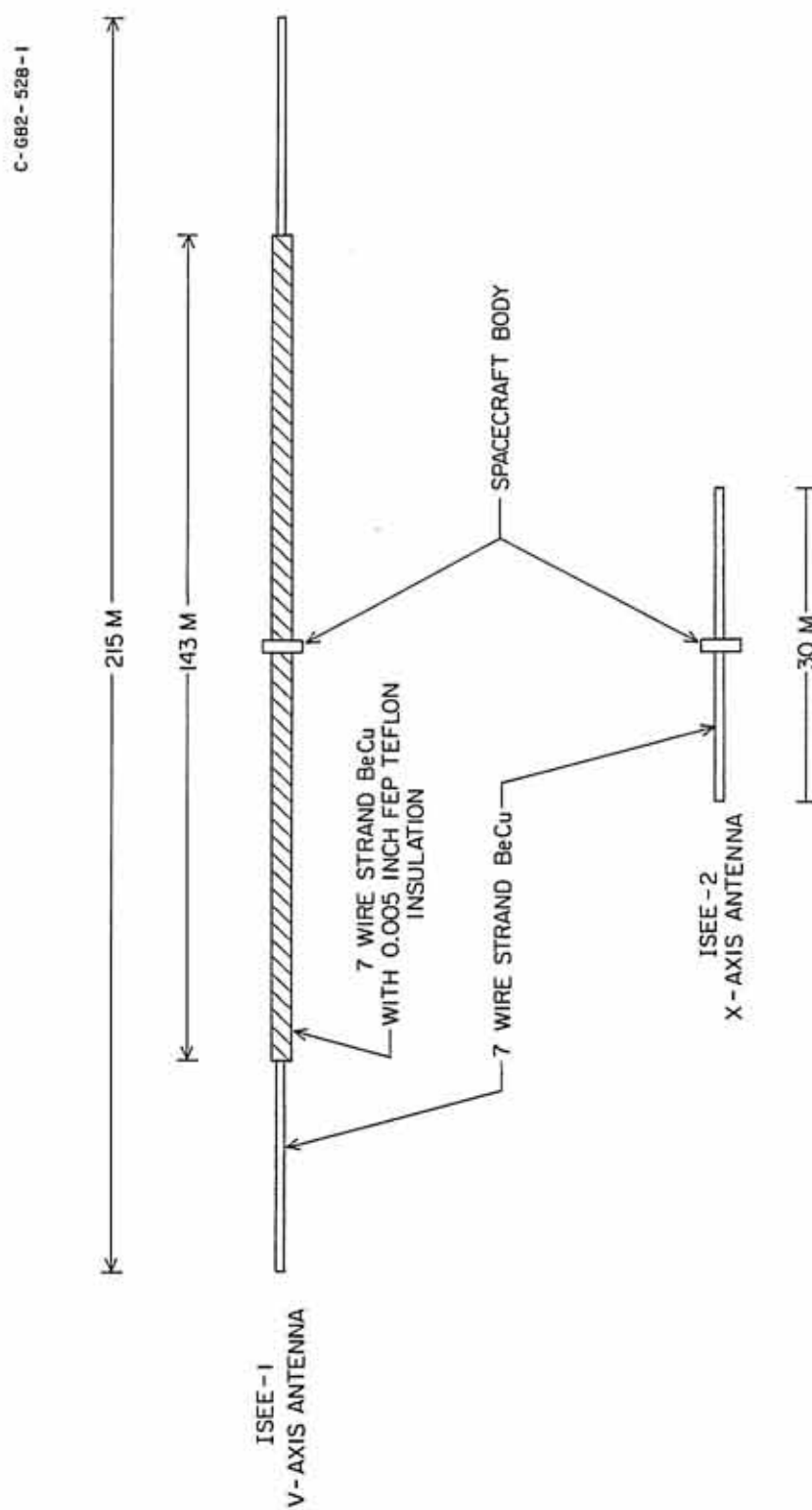
Figure 2

Figure 3   Wideband data from ISEE-1 is shown for November

22, 1977 (day 326) from 9h 57m 0s to 9h 57m 15s.

The spacecraft is located at about 12.4 R_E, 12.9°

magnetic latitude, and 10.9 hours magnetic local

time. Both panels display frequency-time spectro-

grams; the upper panel from 0 to 10 kHz and the

lower panel from 0 to 1 kHz. The 10 kHz channel

has a low frequency instrument cutoff at 650 Hz and

data below 150 Hz in the 1kHz channel has been

eliminated in order to enhance the shading of the

higher frequencies. In the interval from 6 seconds

to 9 seconds, the festoon-shaped emission bandwidth

varies from 200 Hz-800 Hz at about 6.5 seconds

to 400 Hz - 2k Hz at about 7.5 seconds.
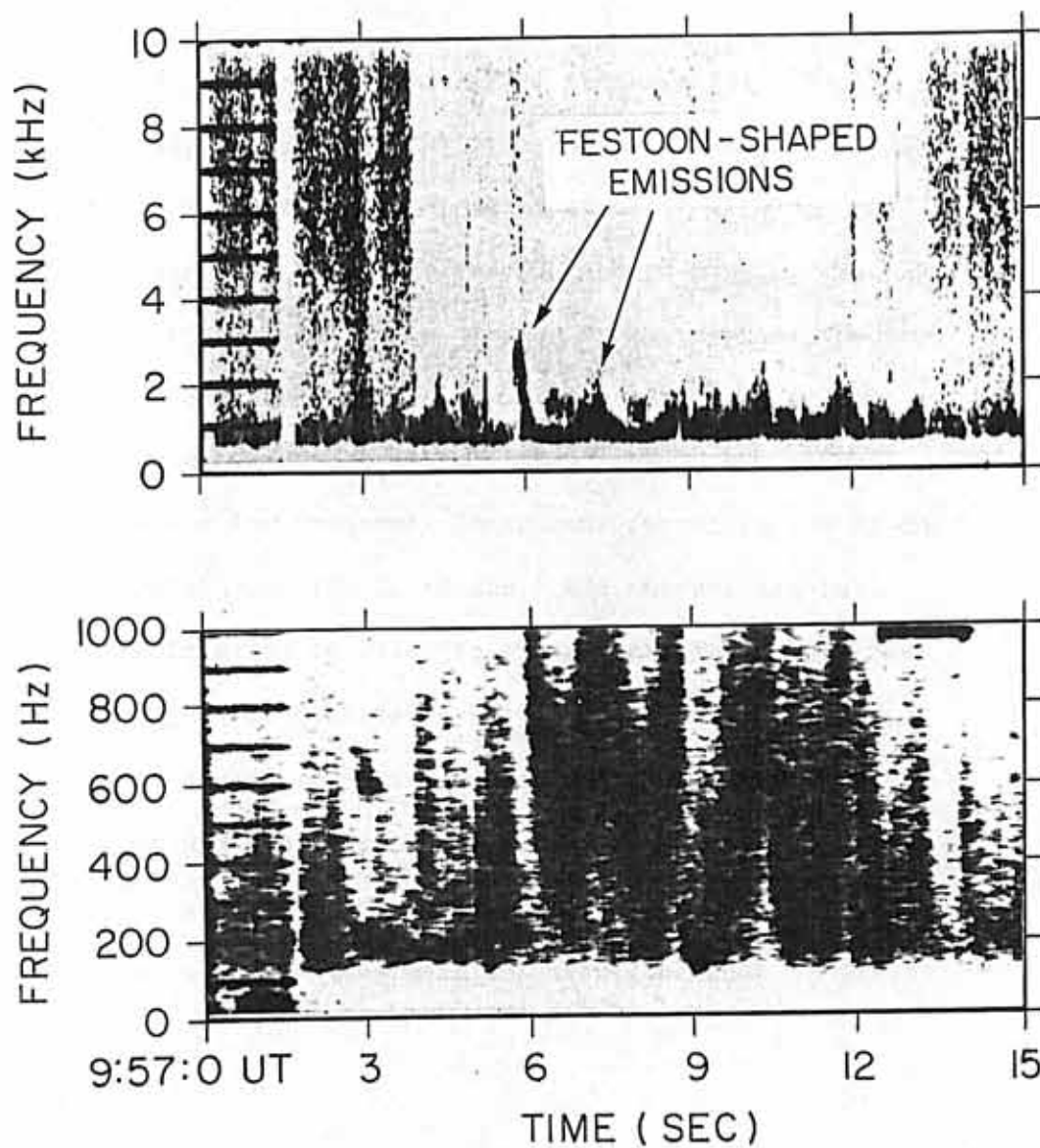
B-G82-410-1

ISEE-1 WIDEBAND DATA
YEAR 1977 DAY 326

FIGURE 3

Figure 4   Wideband data from ISEE-1 is shown for November
            22, 1977, (day 324) from 9h 57m 15s to 9h 57m 30s.
            The spacecraft is located at about 12.4 R_E, 12.9°
            magnetic latitude, and 10.9 hours magnetic local
            time. Both panels display frequency-time spectro-
            grams; the upper panel from 0 to 10 kHz and the
            lower panel from 0 to 1 kHz. The 10 kHz channel
            has a low frequency instrument cutoff at 650 Hz and
            data below 150 Hz in the 1 kHz channel has been
            eliminated in order to enhance the shading of the
            higher frequencies. The emission extends to as
            high as 5 kHz and shows a periodic gap in intensity
            at all frequencies. A second frequency component
            is evident at about 23 seconds, however, it may be
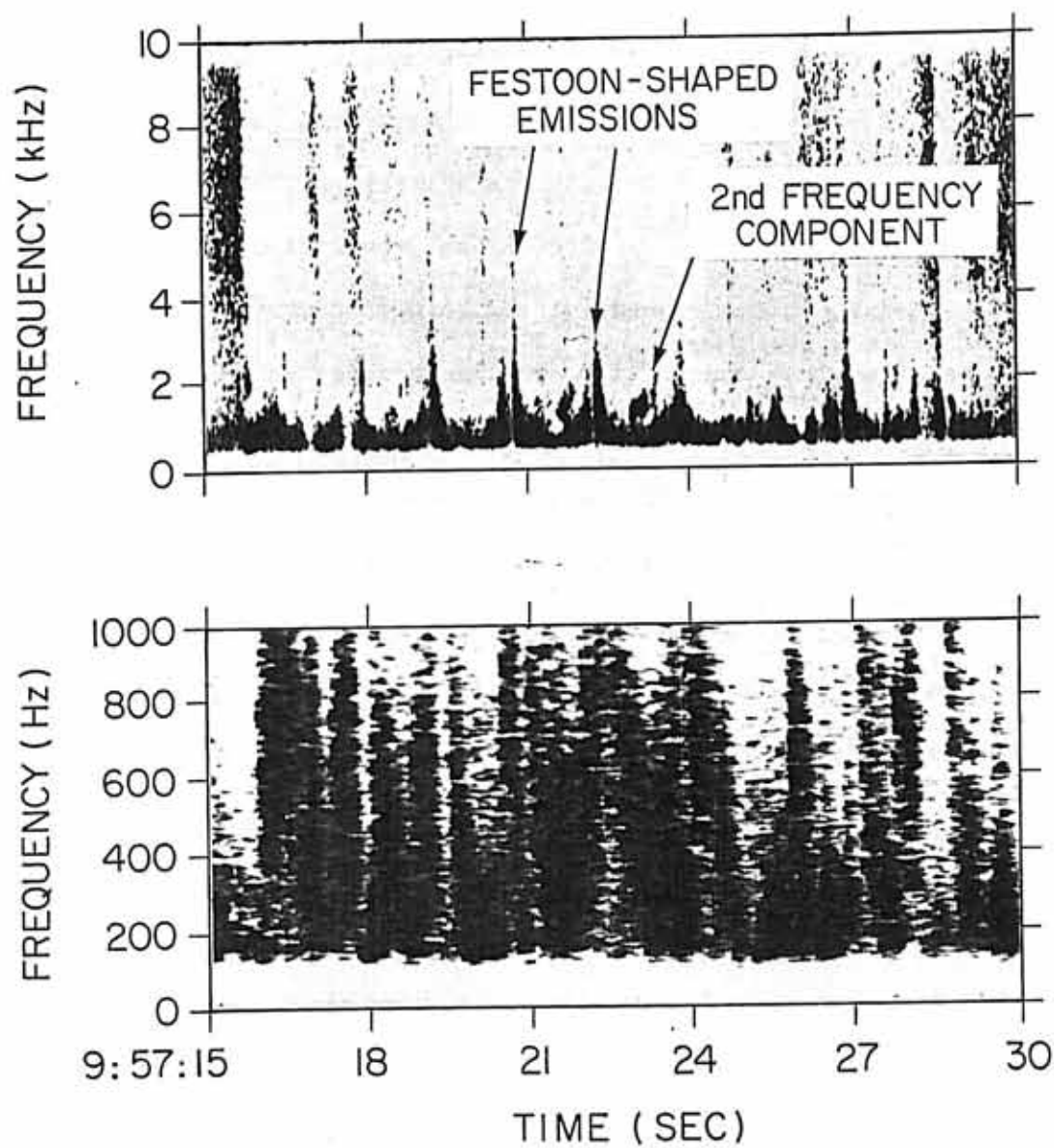   unrelated to the main emission spectrum.

B-G82-411-1

ISEE-1 WIDEBAND DATA
YEAR 1977 DAY 326

FIGURE 4

Figure 5   Wideband data from ISEE-1 is shown for November 22, 1977 (day 326) from 9h 59m 30s to 9h 59m 45s. The spacecraft is located at about 12.3 R_E, 12.9° magnetic latitude, and 10.9 hours magnetic local time. panels display kHz frequency-time spectrograms; the upper panel from 0 to 10 kHz and the lower panel from 0 to 1 kHz. The 10 kHz channel has a low frequency instrument cutoff at 650 Hz and data below 150 Hz in the 1 kHz channel has been eliminated in order to enhance the shading of the higher frequencies. The frequency-time structure rises as high as 6 kHz, showing gaps in intensity near 37 seconds and 39 seconds.
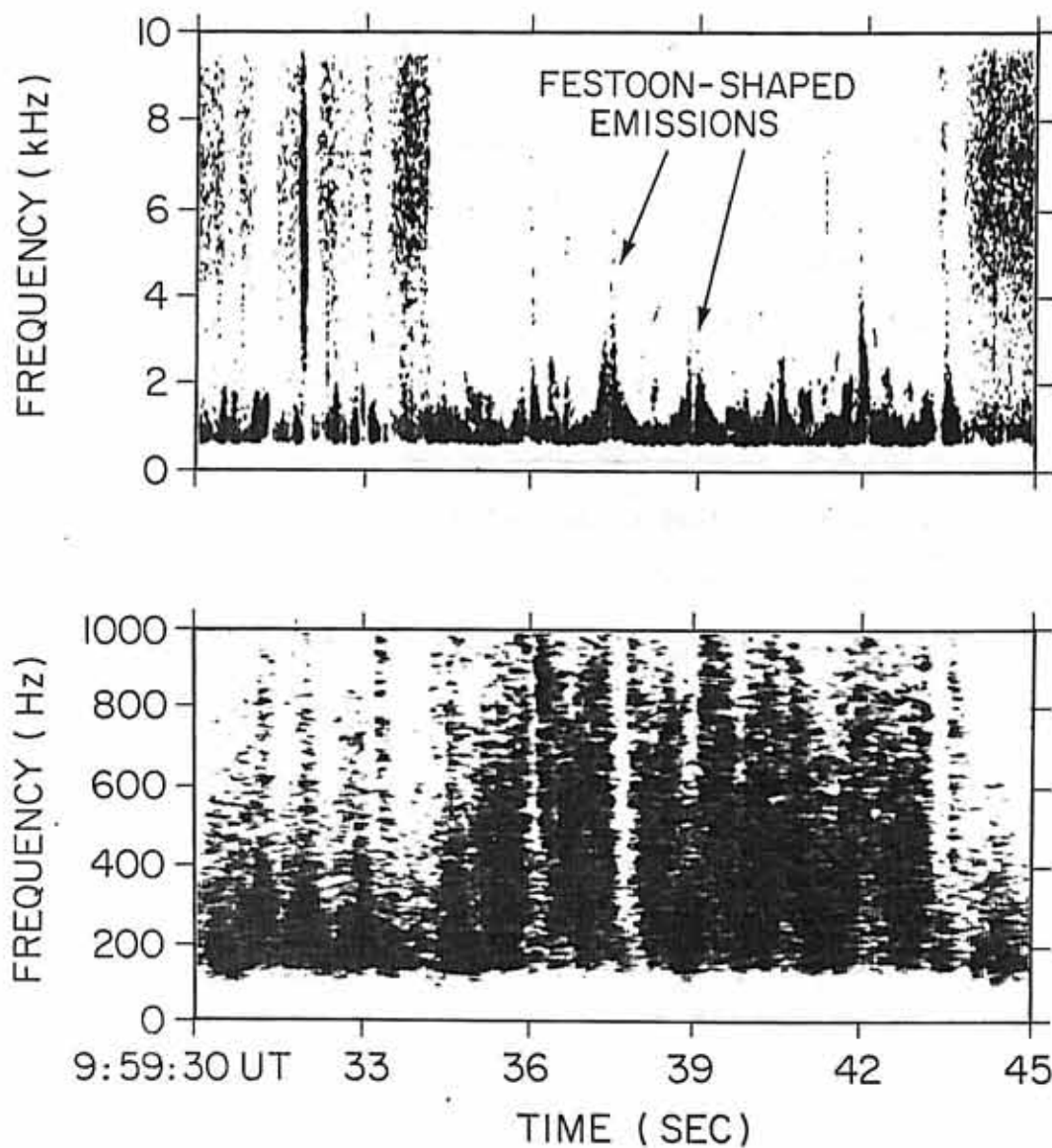
ISEE-I WIDEBAND DATA
YEAR 1977 DAY 326

FIGURE 5

Figure 6   Spectrum analyzer data for November 22, 1977 are

shown for the electric field antenna. Each channel.

covers a dynamic range of 100db. Spacecraft coor-

dinates are shown at the bottom of the panel in

geocentric magnetospheric coordinates. Bow shock

and magnetopause are marked to delineate the pass-

age of the spacecraft through the magenetosheath,

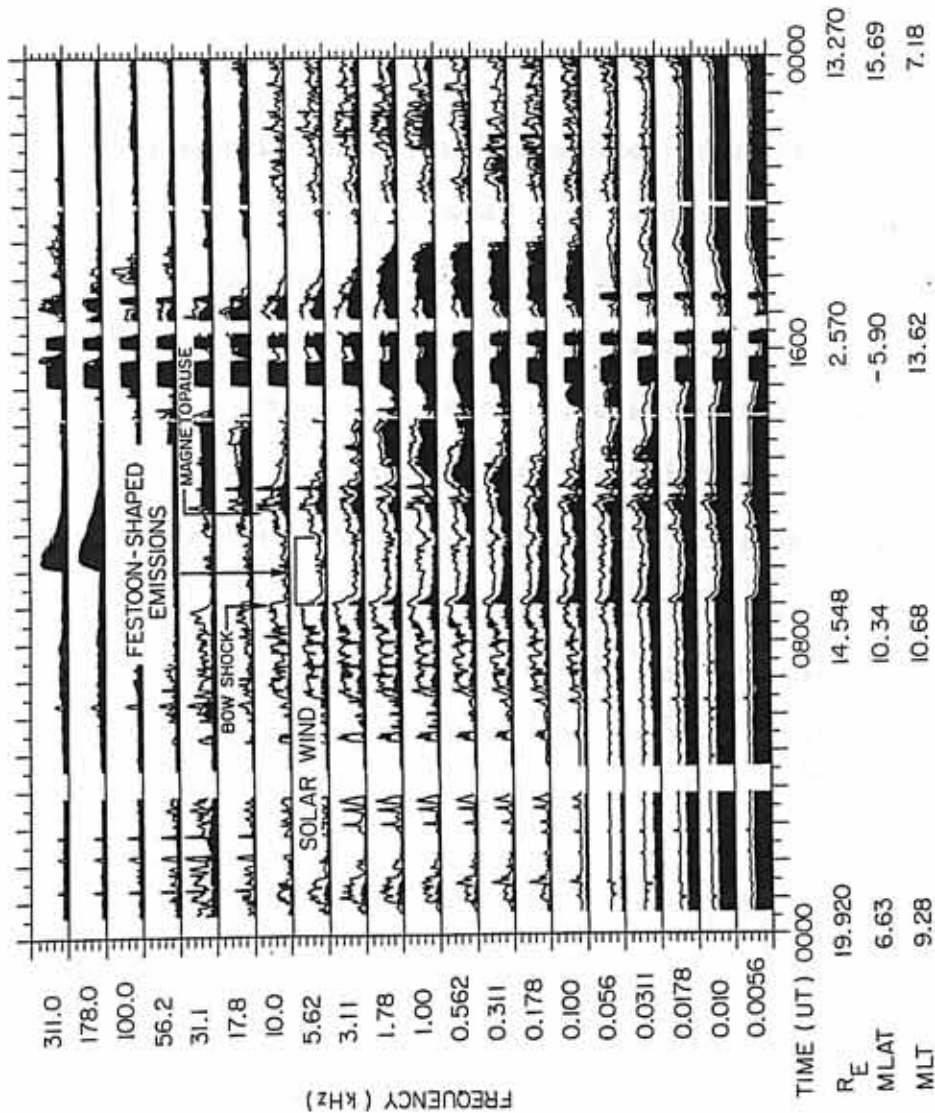where the festoon-shaped events are studied.

C-GB2-508-2

NOVEMBER 22, 1977 DAY 326

FESTOON-SHAPED
EMISSIONS

MAGNETOPAUSE

BOW SHOCK

SOLAR WIND

FREQUENCY (kHz)

311.0			
178.0			
100.0			
56.2			
31.1			
17.8			
10.0			
5.62			
3.11			
1.78			
1.00			
0.562			
0.311			
0.178			
0.100			
0.056			
0.0311			
0.0178			
0.010			
0.0056			

TIME (UT)	0000	0800	1600	0000
R_E	19.920	14.548	2.570	13.270
MLAT	6.63	10.34	-5.90	15.69
MLT	9.28	10.68	13.62	7.18

FIGURE 6

Figure 7   The magnetic field and plasma flow velocities are
            shown in geocentric solar magnetospheric coordi-
            nates for the event times in Figures 3, 4, and 5.
            The center graph is a two-dimensional representa-
            tion of the three-dimensional orientations of these
            vectors. The other graphs are projections of the
            vectors into the three orthogonal coordinate
            planes. The X-Y plane contains the rotating elec-
            tric dipole antenna and includes the projected
            magnetic field and plasma flow vectors.

68

ISEE-I PLASMA FLOW/MAGNETIC FIELD ENVIRONMENT
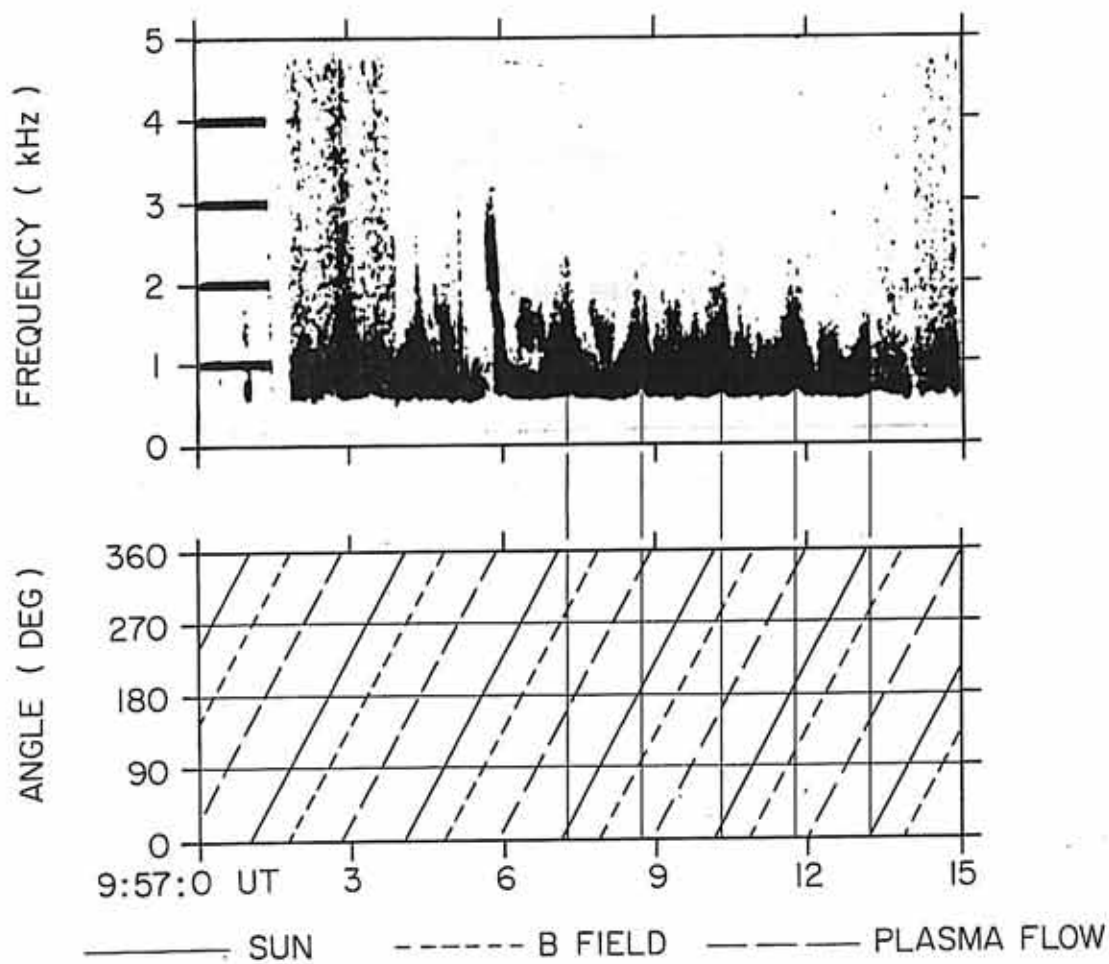
YEAR 1977 DAY 326 09^h:57^{m}UT
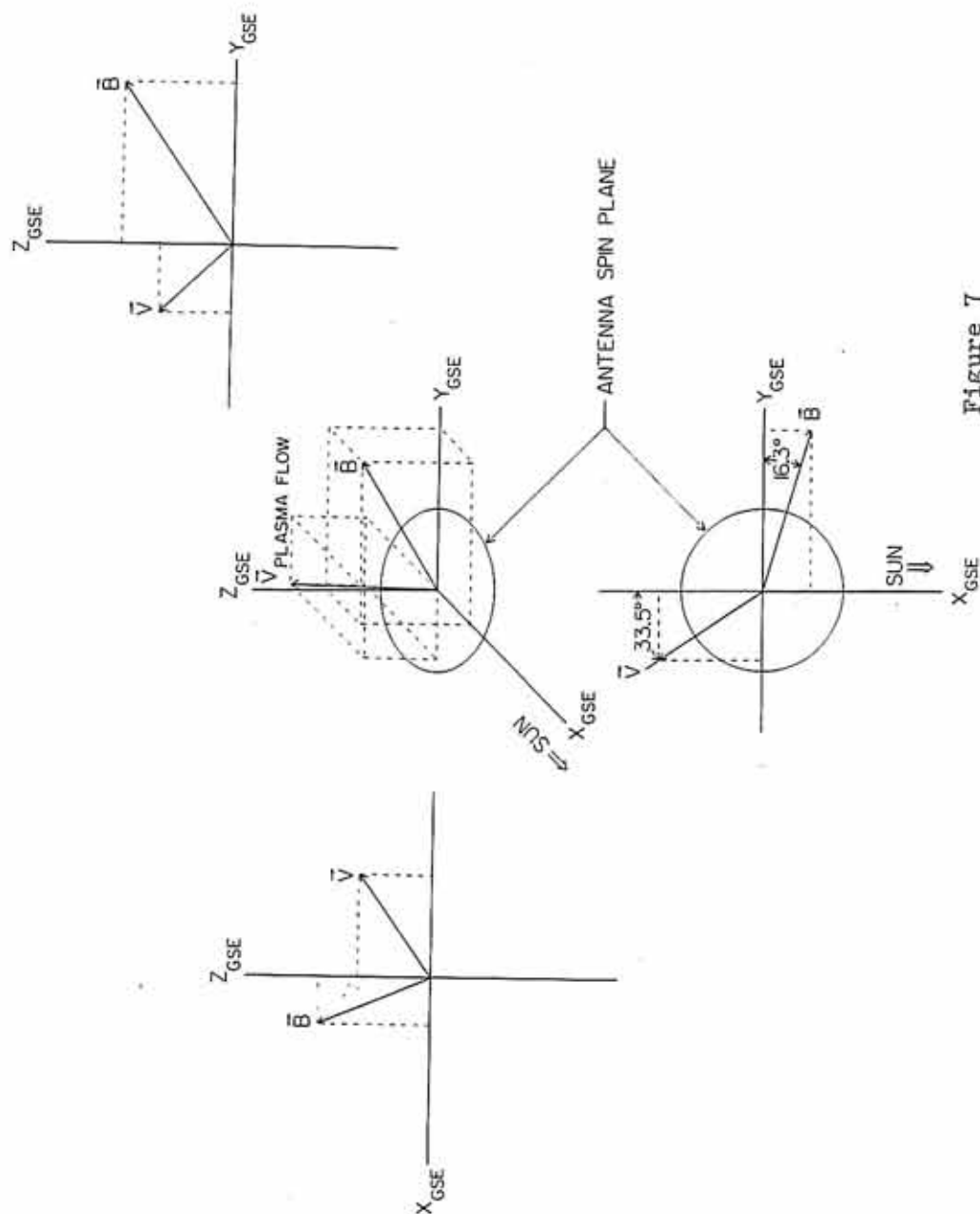
Figure 7

Figure 8   The event time shown in Figure 3 is expanded in frequency and displayed along with the orientation of the spacecraft antenna with respect to the spacecraft-sun line, the magnetic field, and the plasma flow velocity. Vertical reference lines are drawn to determine the antenna orientation when the emission bandwidth is a maximum. For those marked times, the average antenna to magnetic field and plasma flow velocity angles are 104 ±3 degrees and −26 ±6 degrees, respectively.

A-G82-299

ISEE-1 WIDEBAND WAVE DATA AND ANTENNA ORIENTATION
YEAR 1977 DAY 326

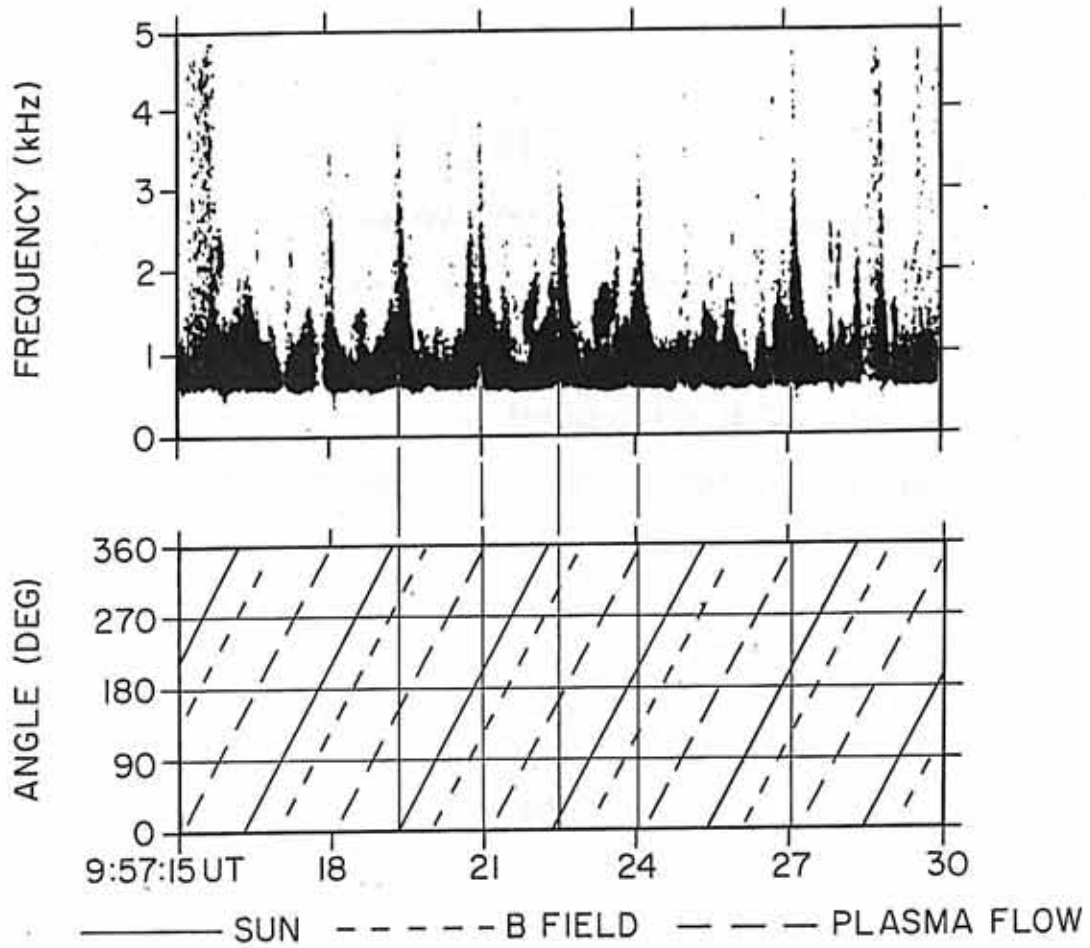
FIGURE 8

Figure 9   The event time shown in Figure 4 is expanded in

frequency and displayed along with the orientation

of the spacecraft antenna with respect to the

spacecraft-sun line, the magnetic field, and the

plasma flow velocity. Vertical reference lines

are drawn to determine the antenna orientation

when the emission bandwidth is a maximum. For

those marked times, the average antenna to

magnetic field and plasma flow velocity angles are

121 $\pm$4 degrees and -14 $\pm$6 degrees, respectively.

A-G82-300

ISEE-I WIDEBAND WAVE DATA AND ANTENNA ORIENTATION
YEAR 1977 DAY 326

FIGURE 9

Figure 10   The event time shown in Figure 5 is expanded in
frequency and displayed along with the orientation
of the spacecraft antenna with respect to the
spacecraft-sun line, the magnetic field, and the
plasma flow velocity. Vertical reference lines
are drawn to determine the antenna orientation
when the emission bandwidth is a maximum. For
those marked times, the average antenna to mag-
netic field and plasma flow velocity angles are 77
±4 degrees and −60 ±6 degrees, respectively.

ISEE-I WIDEBAND WAVE DATA AND ANTENNA ORIENTATION
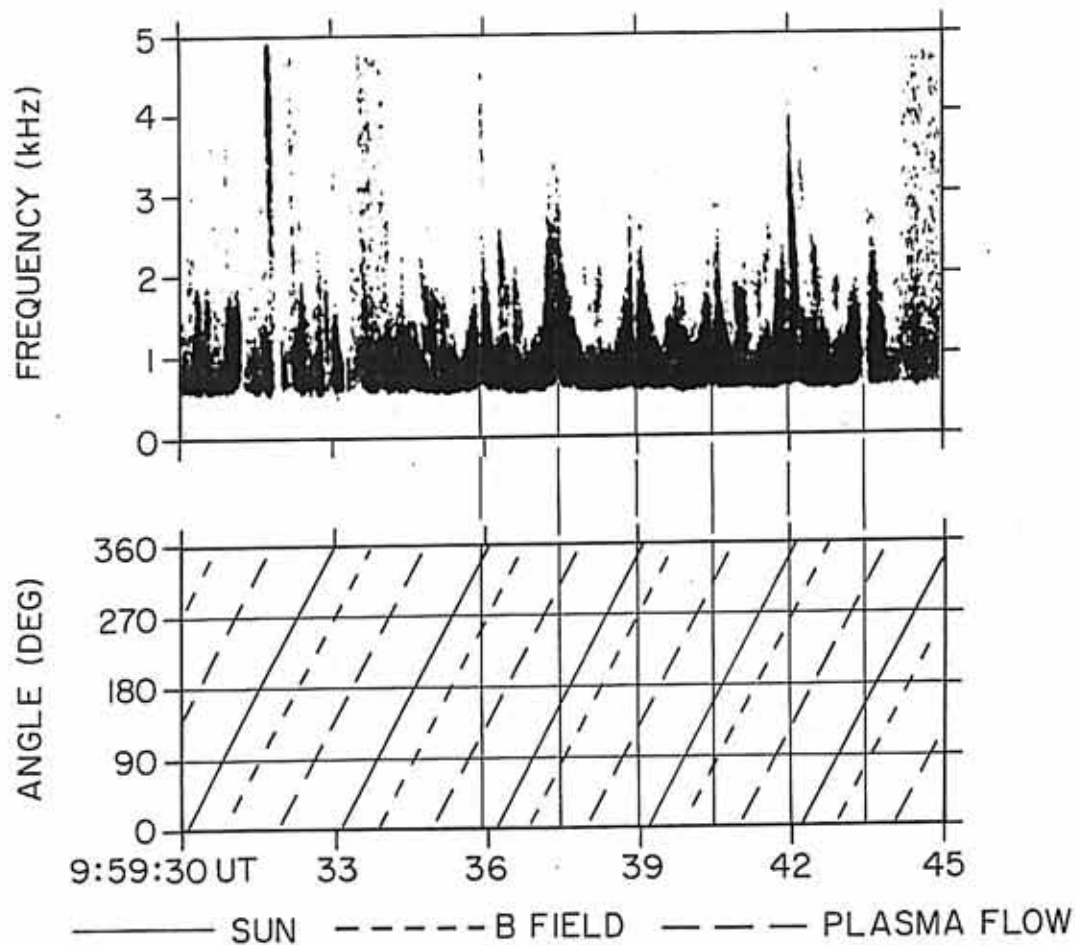YEAR 1977 DAY 326

FIGURE 10

Figure 11   ISEE-1 antenna orientation to the magnetic field

and plasma flow velocities are summarized for the

times marked with vertical lines in Figures 8, 9,

and 10. Orientation angle is found to be reason-

ably constant over time intervals of 6 seconds to

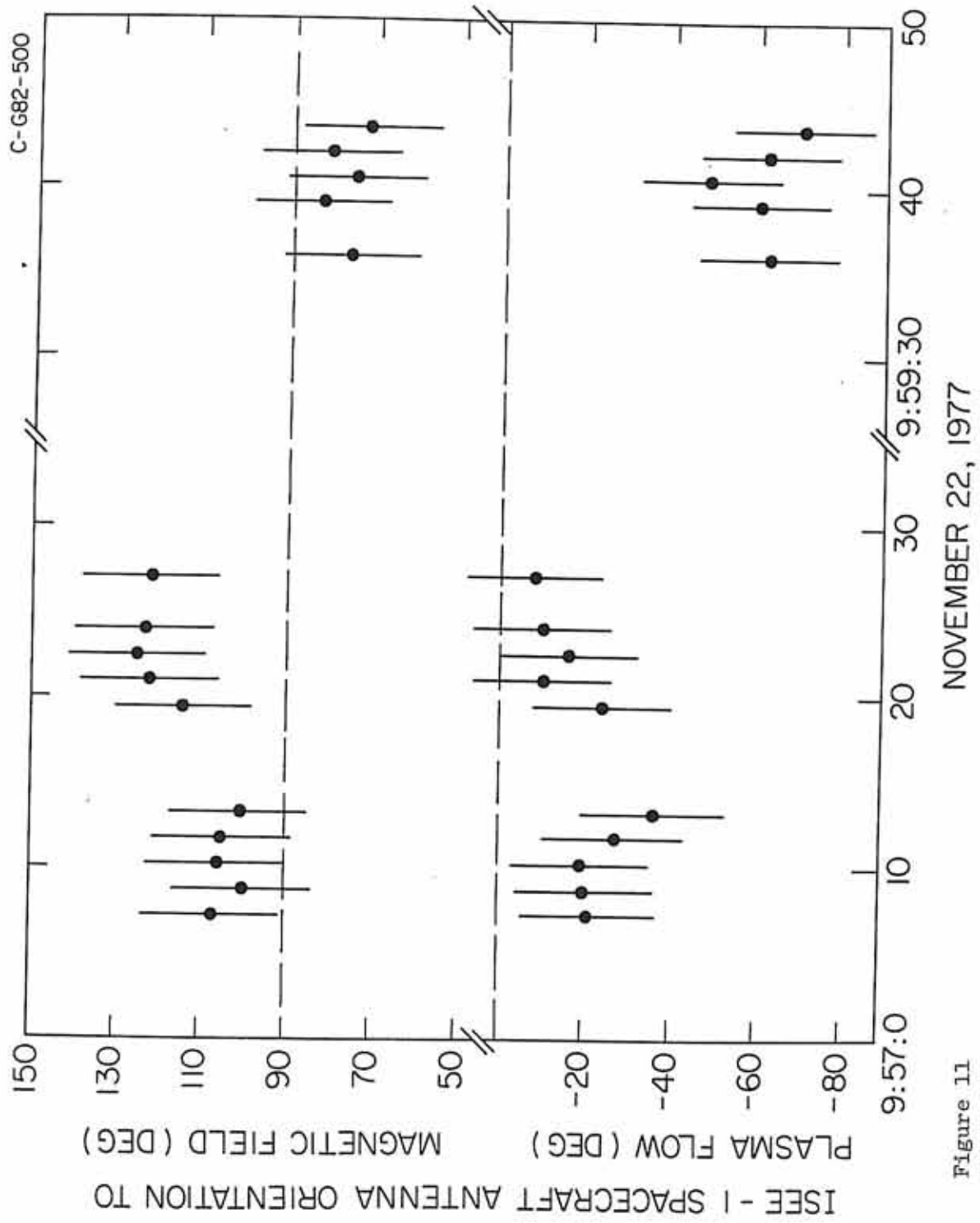10 seconds, however, not coherent over time inter-

vals of 140 seconds or longer.

Figure 11

Figure 12   A portion of the ISEE-1 orbit projected into the

noon-midnight plane in GSE coordinates is shown from

0600 UT to 1400 UT on November 22, 1977. One hour

intervals are marked along the orbit. The bow shock

and magnetopause boundaries have been adjusted

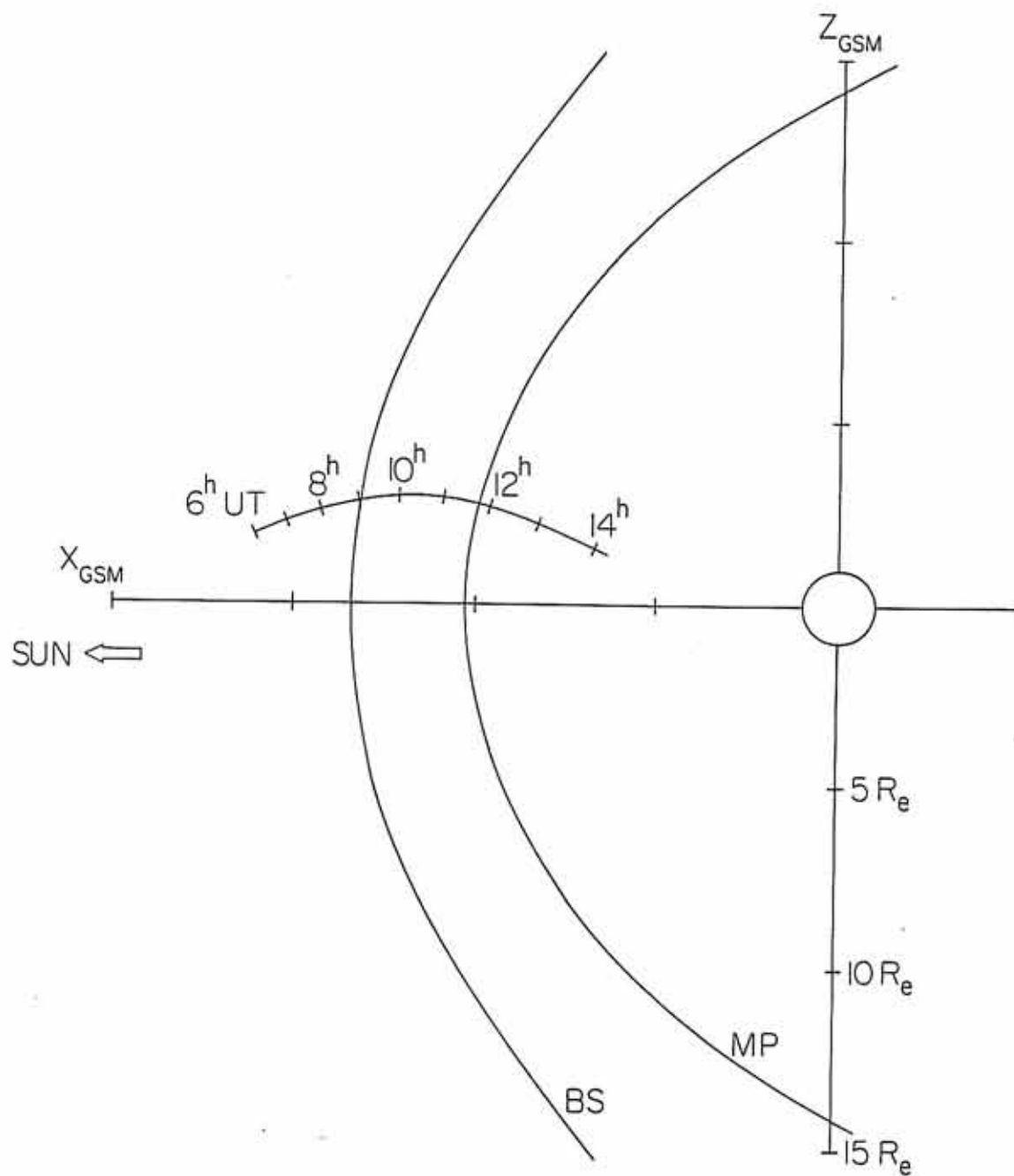to match that observed for this inbound pass.

C-G82-319-1

NOON – MIDNIGHT PROJECTION OF ISEE-1 ORBIT
YEAR 1977 DAY 326

Figure 12

Figure 13   The ISEE-1 orbit for the same times shown in

Figure 12 is projected into the GSM equatorial

plane.   The spacecraft is on an inbound pass near
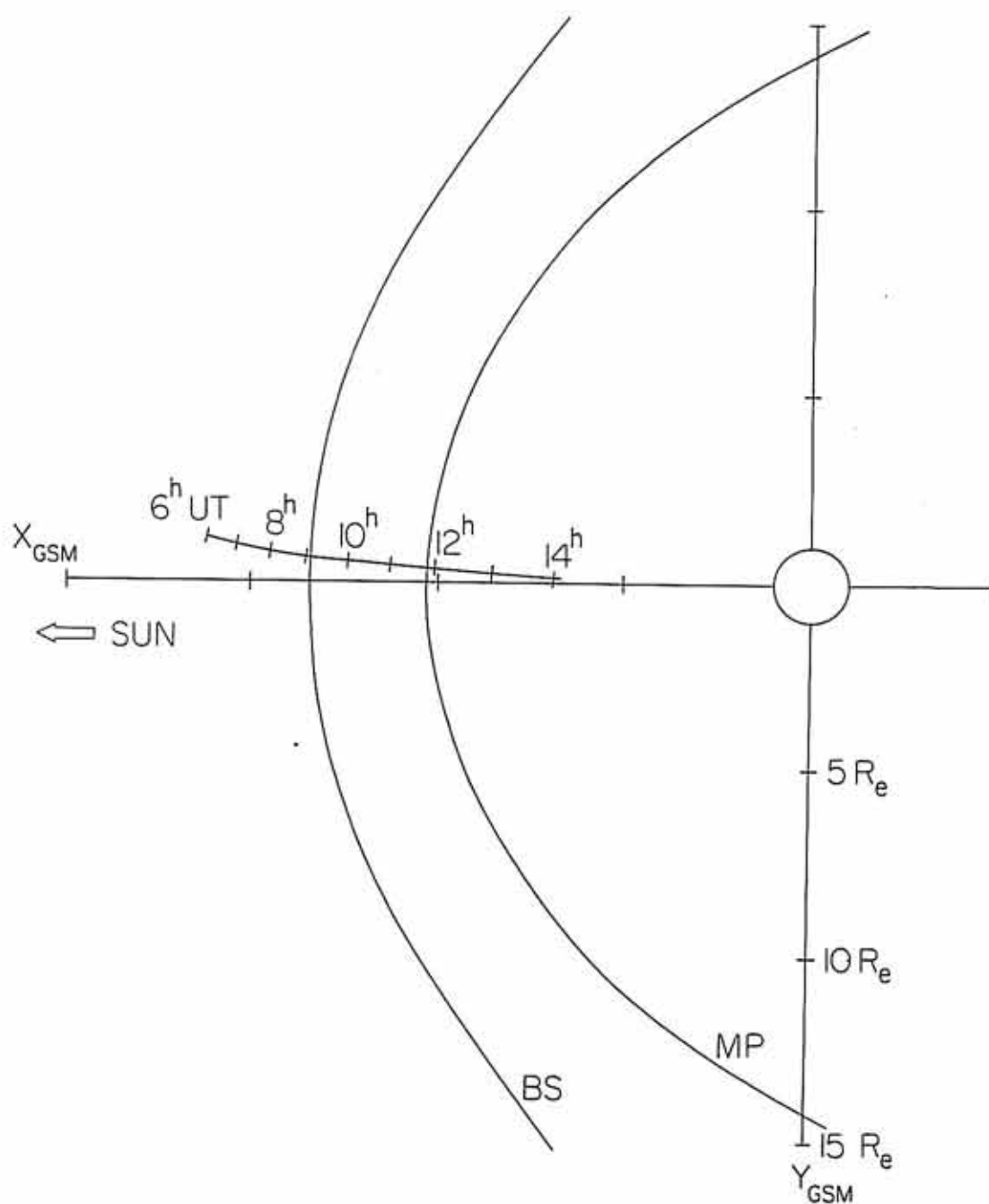
11 hours local time.

C-G82-318

EQUATORIAL PROJECTION OF ISEE-1 ORBIT
YEAR 1977 DAY 326

X_{GSM}

6^h UT 8^h 10^h 12^h 14^h

⇐ SUN

5 R_e

10 R_e

MP

BS

15 R_e

Y_{GSM}

Figure 13

Figure 14   Electric field and wave number vectors are shown
along with angle definitions. These definitions
are those used in developing the antenna response
to a spectrum of wave numbers. The antenna spin-
plane component of $\vec{k}$ is k_ρ and its azimuthal angle
to the GSE coordinate x-axis is α_k. The vector $\vec{\ell}$
is along the electric dipole antenna and θ defines
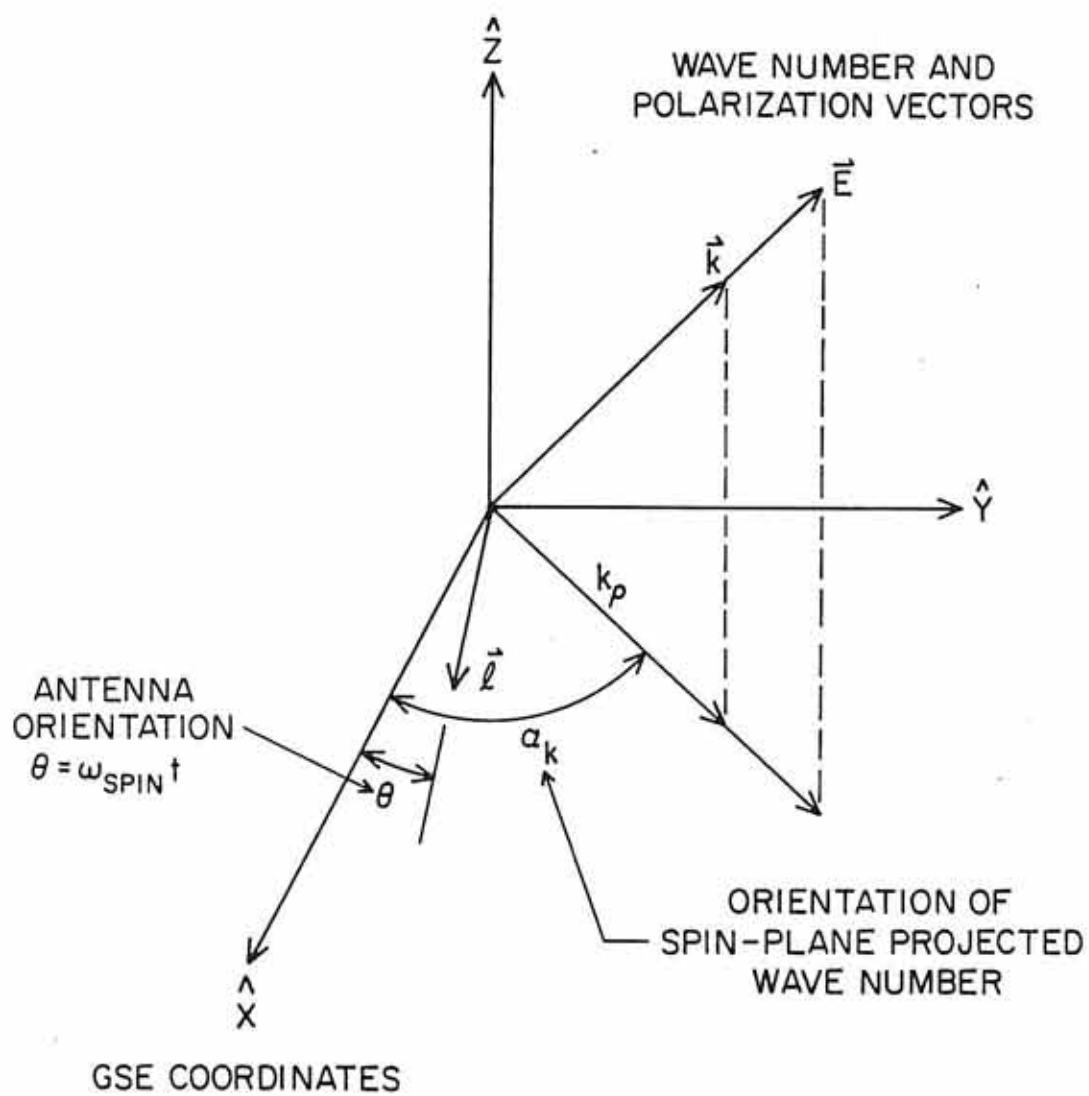its azimuthal orientation.

A-G82-60I

Figure 14

Figure 15   Relative antenna response intensity, for antenna
orientation along the polarization electric field,
as a function of wave number and for two parameter
conditions are shown. For $L_1=1$ meter, the intensity
is power law with spectral index of −4 at wavelengths
less than the antenna length. For $L_1=143$ meters
the fall-off in intensity is more rapid than power
law. The smaller value is appropriate for capaci-
tive antenna coupling to the plasma and the larger
value, for resistive coupling. For magnetosheath
conditions, the antenna is thought to couple
capacitively to the plasma ($L_1 = 1$ meter).

C-GB2-510-2

WAVELENGTH (METERS)

RELATIVE AMPLITUDE

$K_\rho L_2/4$ (RADIANS)

L_2

NONLINEAR SLOPE

$L_1 = 143$ METERS
$L_2 = 215$ METERS

L_2

LINEAR SLOPE = -4

$L_1 = 1.0$ METERS
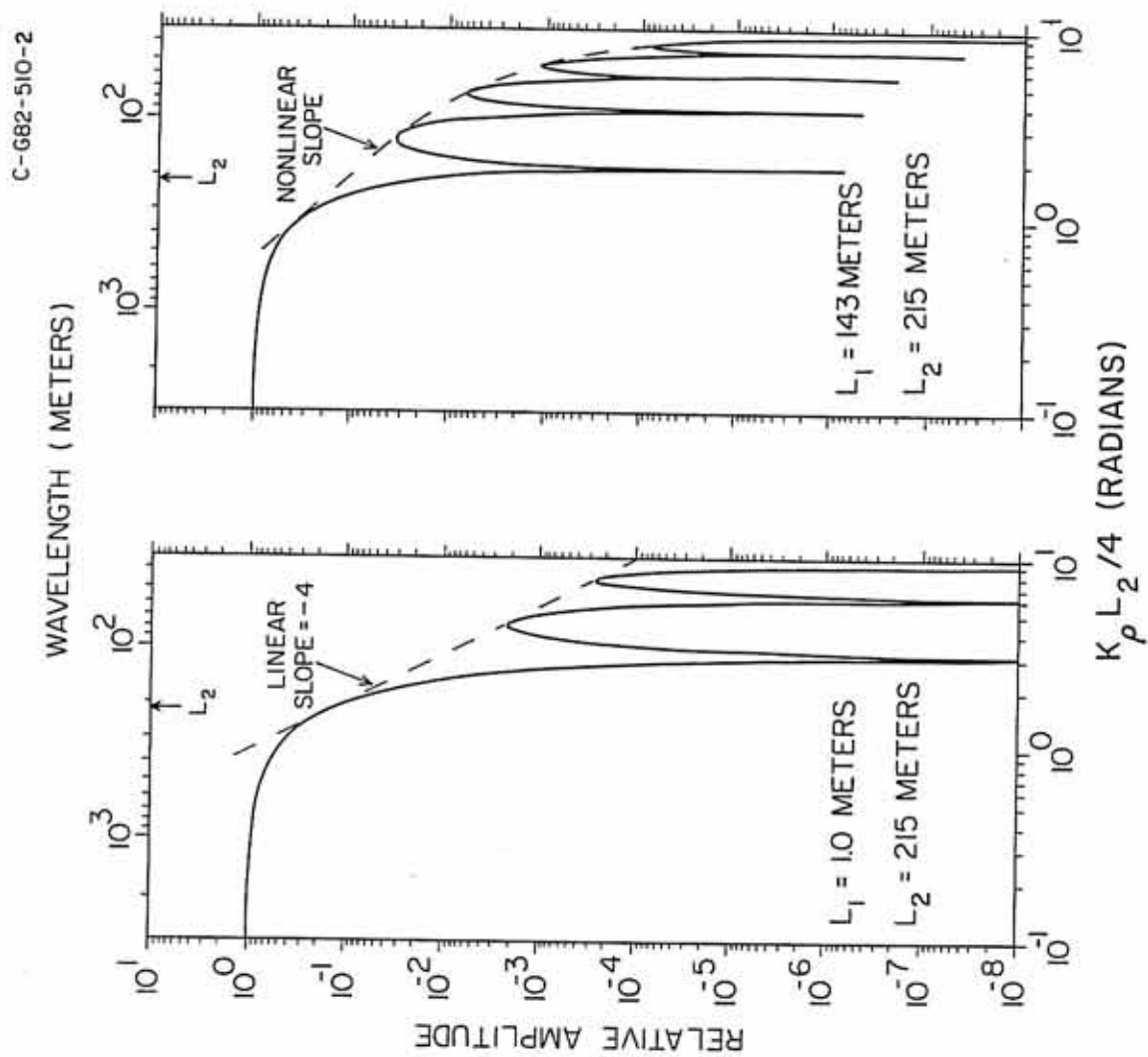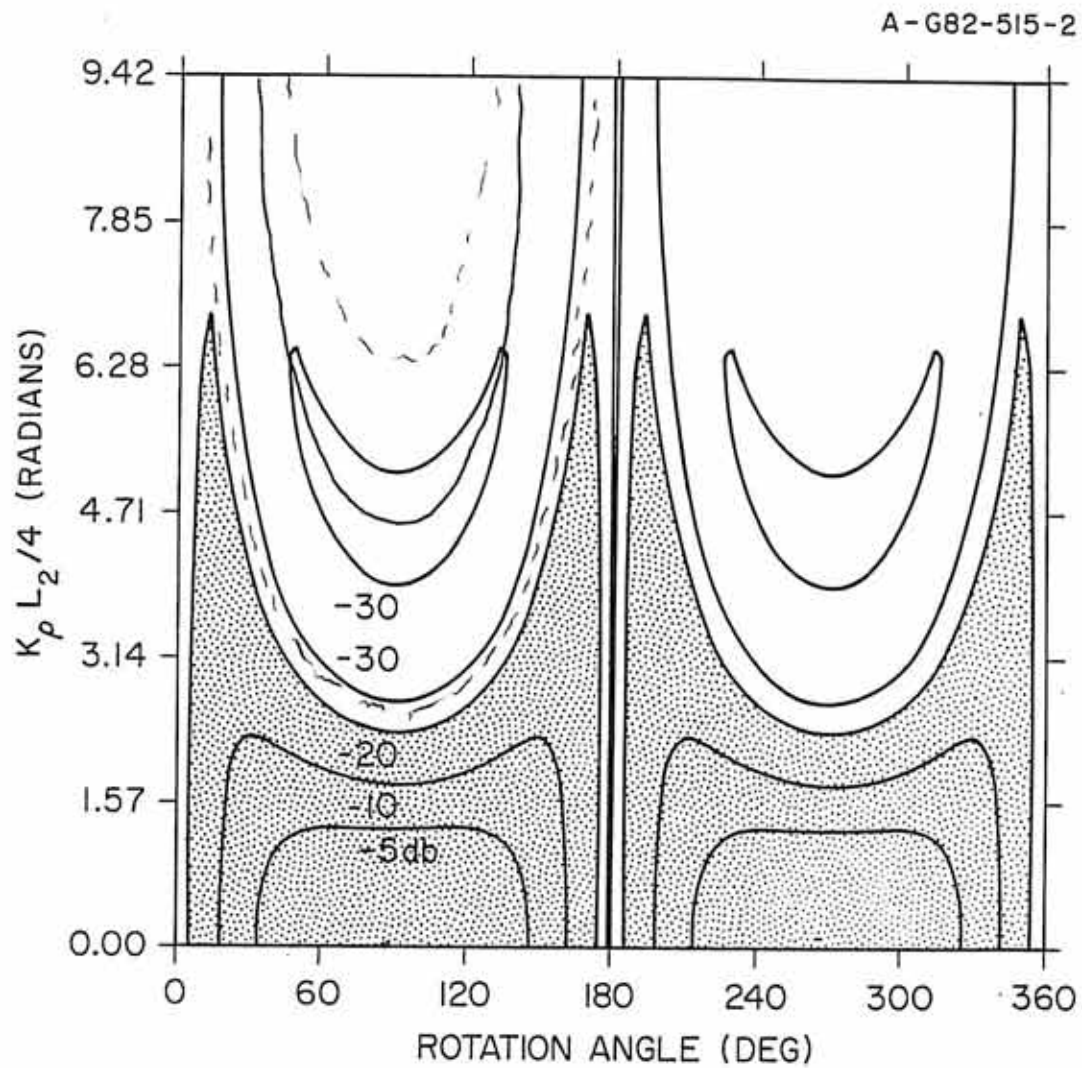$L_2 = 215$ METERS

Figure 15

Figure 16   Antenna model response to a spectrum of wave numbers

is summarized. Contours trace equal intensity

levels at labeled decibel values referenced to the

peak value. The model qualitatively reproduces the

emission festoon-shape and the intensity gap at all

frequencies for antenna orientations perpendicular

to the polarization electric field. The wave number

and electric field vectors are both at $\theta = 90°$ for

the purpose of illustrating the antenna response to

a spectrum of wave numbers.

Figure 16

Figure 17   Antenna response intensity contours are compared
             directly to an event observed with the wideband
             receiver. Measurement of the antenna orientation to
             the projected vector wave number determines horizon-
             tal registration with the antenna response contours
             and spectral shape is used to obtain vertical regis-
             tration. The contour lines are found to reproduce
             the festoon-shape spectrum and also reflect the shape
             of the intensity gap at about 38.95 seconds. The
             intensity dropout is about 5 degrees wide in space-
             craft rotation at 1.3 kHz and widens to 15 degrees
             at about 2 kHz. The match between model antenna
             response and the festoon-shaped emission determines
             a linear relationship between observed frequency and
             magnitude of the spin-plane projected component of
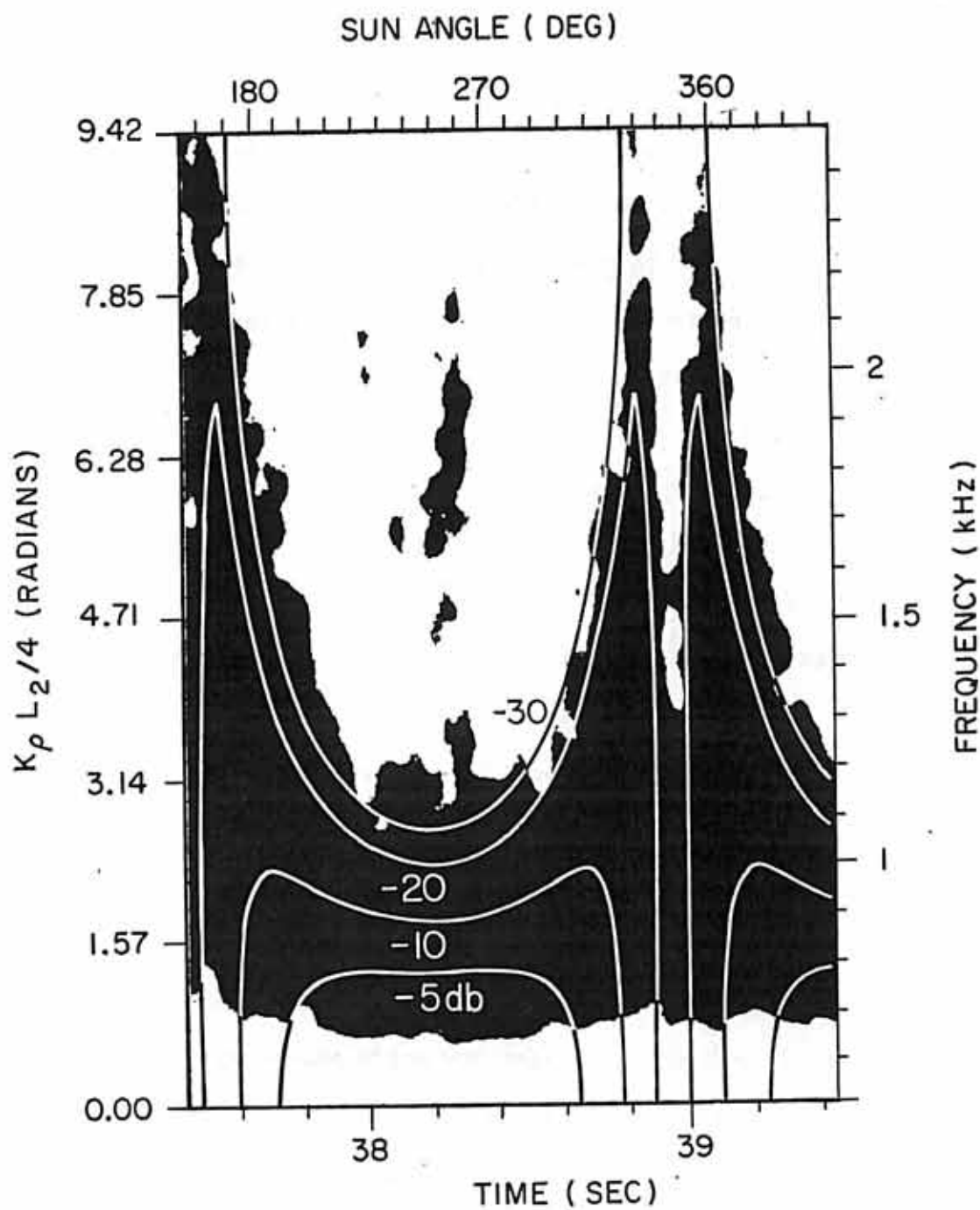   the wave number (k_ρ).

A-G82-572-2

FIGURE 17

Figure 18   The values of wave number and frequency which are

allowed for selected magnitudes of the spin-plane

projected wave number (k_ρ) are plotted. For each

value of k_ρ, two curves result. As shown in the

inset, one curve corresponds to k_ρ chosen to lie in

the dusk half plane of the GSE X-Y plane (α_k = 64

degrees) and the other corresponds to k_ρ in the

dawn half plane (α_k = 244°). The curve is formed

by varying k_z from $-\infty$ to $+\infty$ and computing total

wave number and frequency from Equation 21. For k_ρ

in the dawn half plane, there are no solutions for

$k_z > 0$. Four families of curves are plotted corre-

sponding to values of k_ρ which cover the modeled

range 1.59×10^{-4} cm^{-1}, 3.5×10^{-4} cm^{-1}, 7.8×10^{-4}

cm^{-1}, and 1.75×10^{-3} cm^{-1}. The more lightly

shaded regions correspond to wave number and fre-

quency values which can only be reached by one of

the α_k values. The more darkly shaded region is

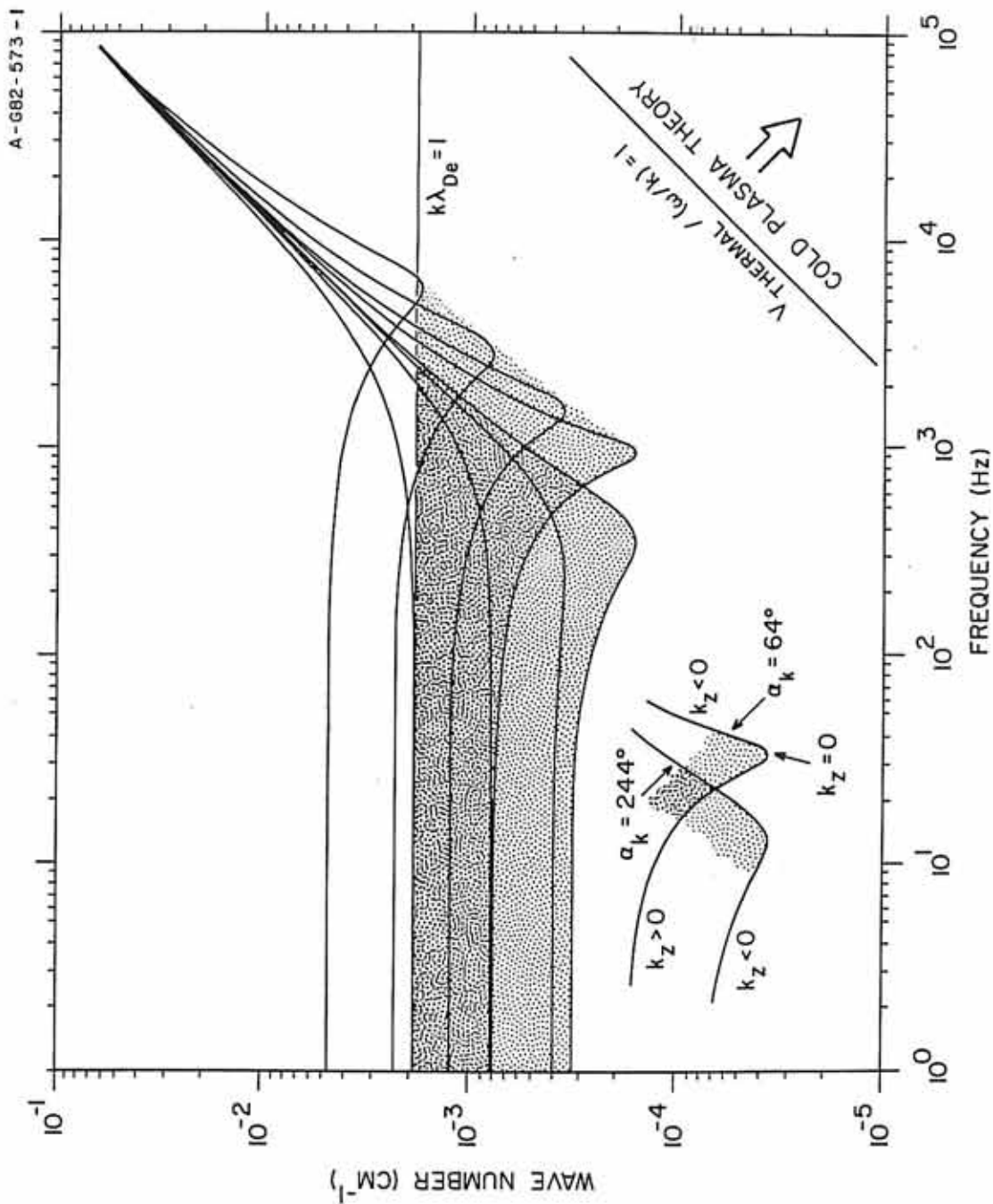accessible for α_k equal to 64° or 244°.

Figure 18

Figure 19   All cold plasma wave mode dispersion curves are

shown for the plasma parameters defined in Appendix

A. Wave number angles to the magnetic field from

0° to 90° sweep out regions which are shaded to

reflect the sense of polarization for electromagnetic
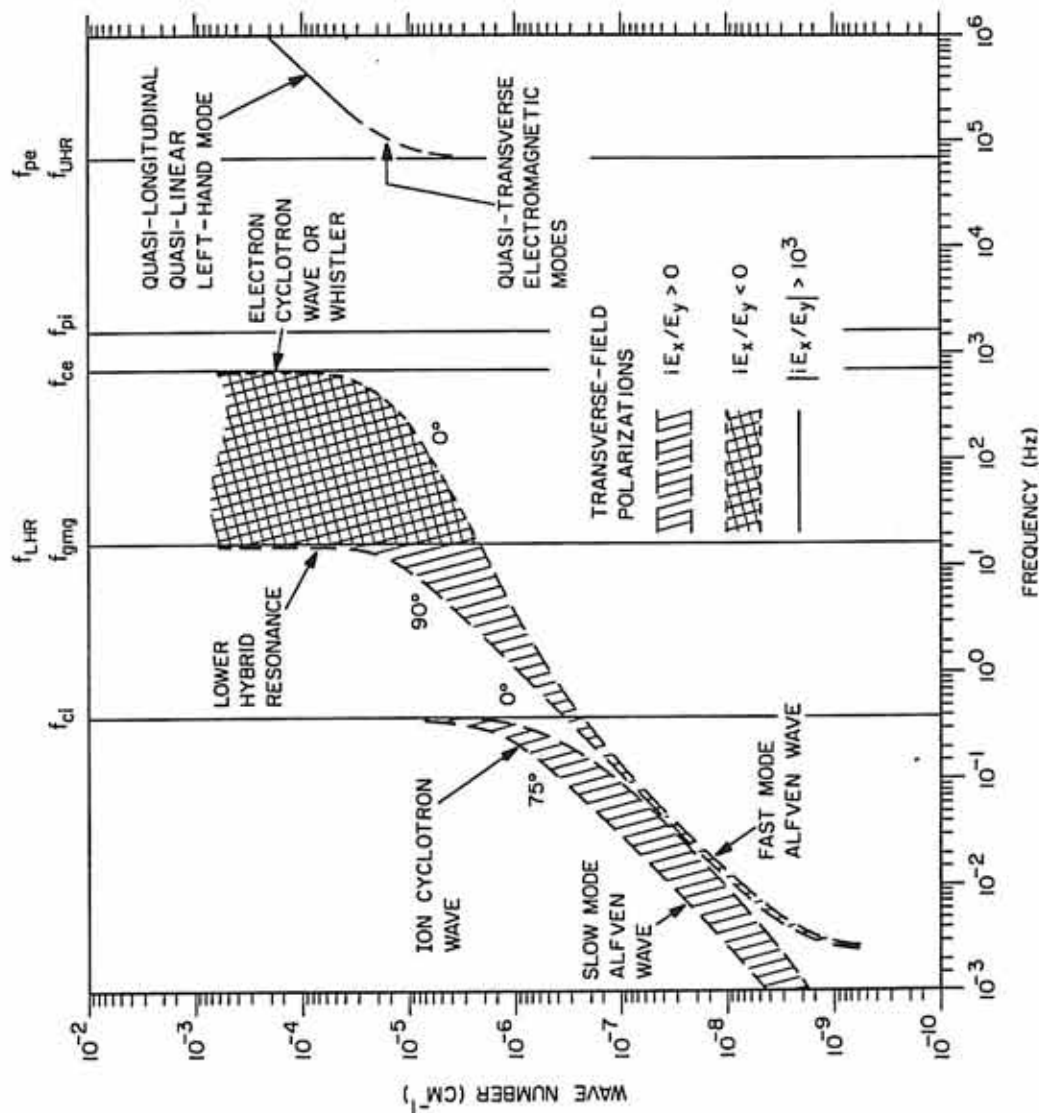
waves. Quasi-linear polarization is shown as a

solid line.

Figure 19

Figure 20 The spin-plane geometry corresponding to the modeled

event in Figure 17 is shown. The projected plane

which must contain the vector wave numbers is at an

angle of 64 degrees to the sun direction in the GSE

X-Y plane. The projected plasma and magnetic field

vectors are also shown.

A-G82-580

EVENT GEOMETRY FOR
NOVEMBER 22, 1977 9^h 59^m 37.4^s – 39.4^s

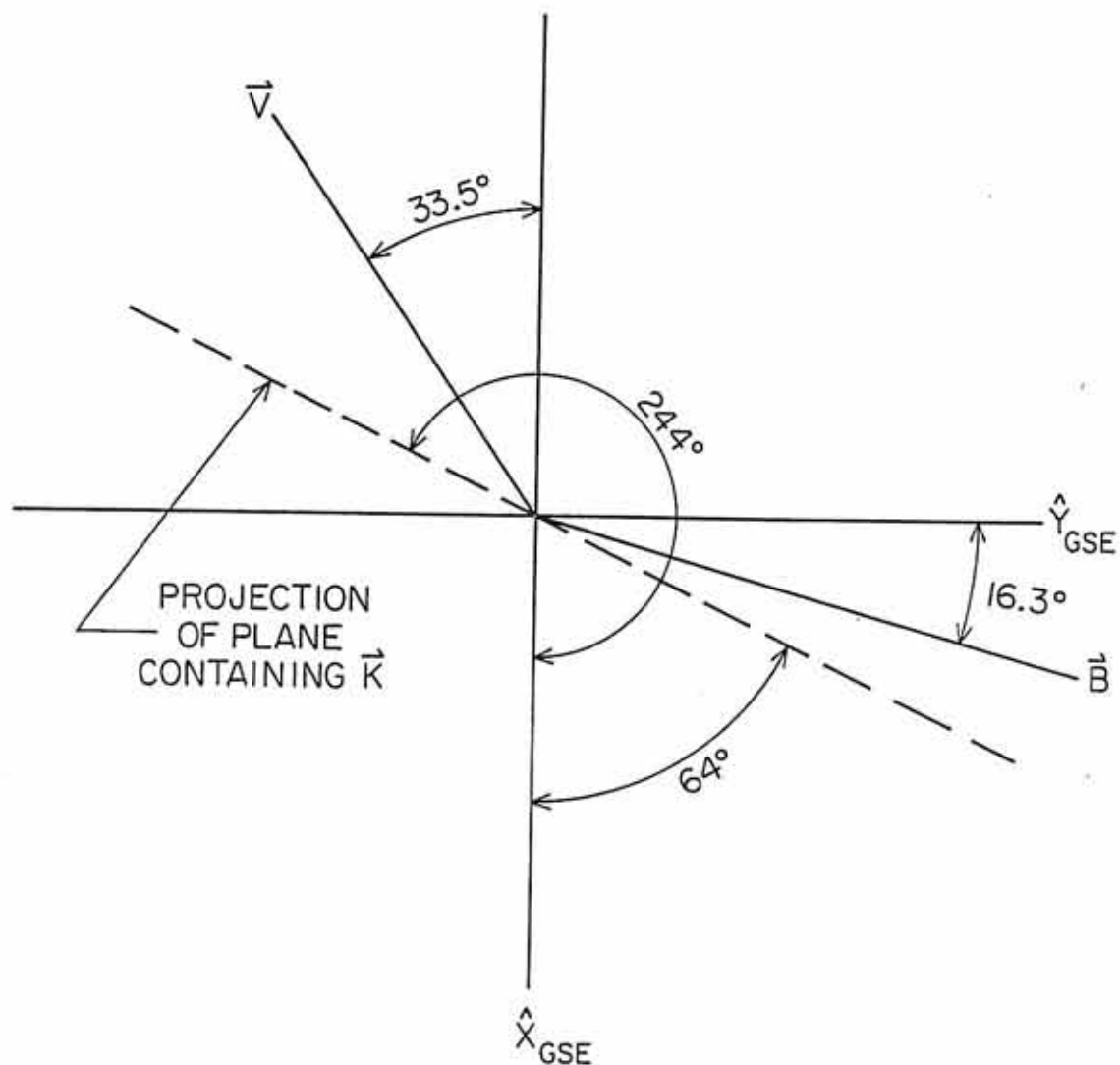
Figure 20

Figure 21   The whistler wave mode satisfies the required wave
              number spectrum (k_ρ) only at a resonance cone, the
              roots of the solutions for the largest wave numbers
              consequently known to exist are plotted. Resonance
              cone angles which require $|\vec{k}|$ to be very near or
              larger than the electron gyroradius ($k\lambda_{De} = a_{ce} \approx$
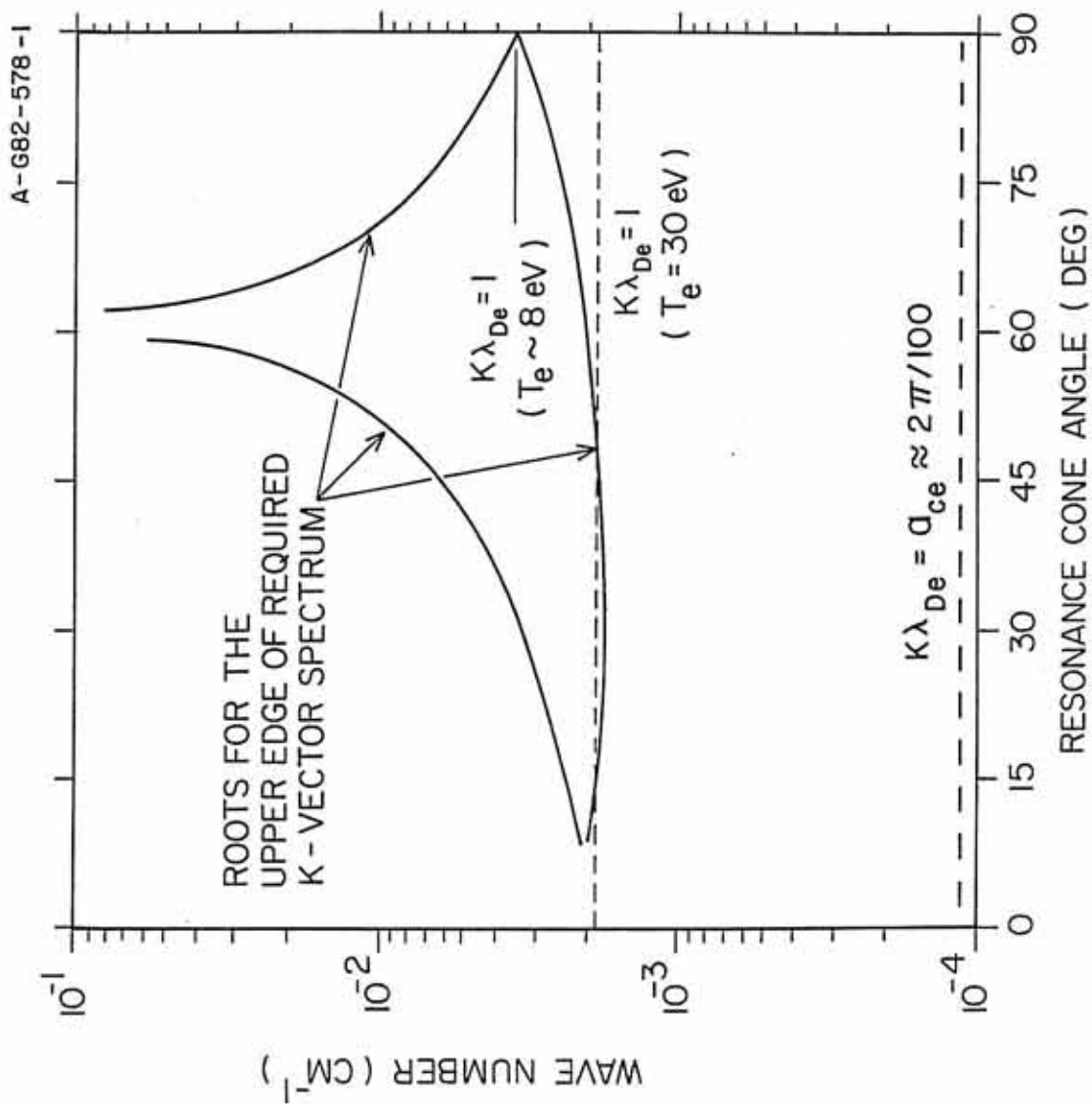 $2\pi/100$) will be strongly damped.

Figure 21

Figure 22 Three-dimensional electron and proton particle

distributions at energies from 215 eV to 45 keV are

displayed. Measurements are from the University of

Iowa quadrispherical plasma analyzer (or LEPEDEA)

on board ISEE-1. Panels 1P through 7P are energy

vs phase angle plots of detector responses for ions

and panels 1E through 7E are the corresponding

plots for electrons. Detectors 1 through 7 have

look-angles ranging from northward to southward-

looking, respectively, with detector 4 centered on

the ecliptic plane. Each panel displays energy and

sample time vertically and azimuthal spin angle

horizontally. Particle intensities are displayed

with color varying from deep blue for the minimum

particle fluxes and bright red for the largest (see

Frank et al., [1978] for further details). The

distributions for both electrons and ions are typi-

cal of near subsolar magnetosheath flows. Pre-

dominantly anti-sunward ion flow is evident as an

intensification near the center of the 5P and 6P
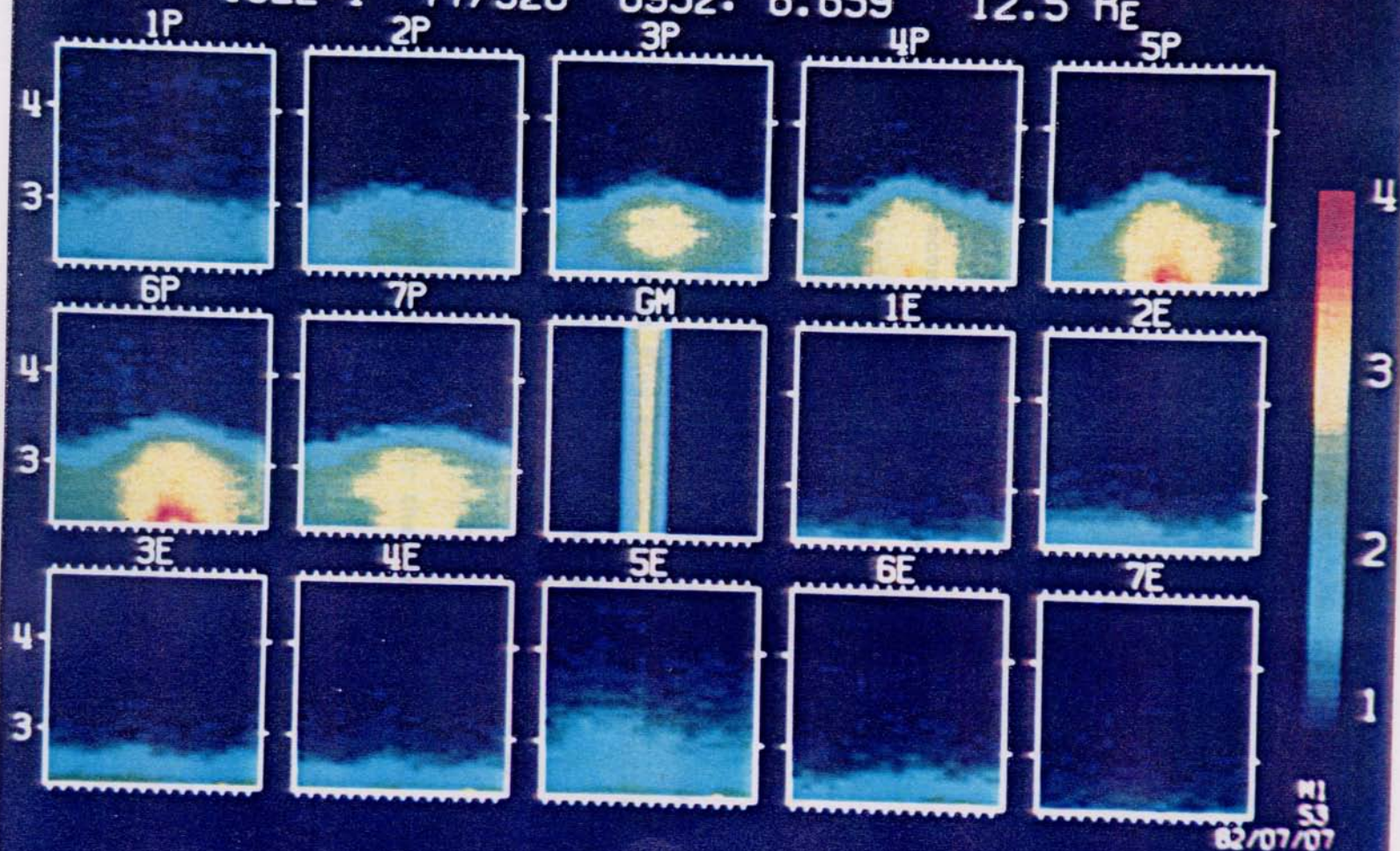
panels.

FIGURE 22

Figure 23   The ion-acoustic mode dispersion equation is plotted against the allowed values of wave number and frequency from Figure 18. Before resonance at the ion plasma frequency, the dispersion curve crosses allowed wave numbers from about 150 Hz to 1 kHz. For plasma flow relative to the spacecraft of about 156 km/s and maximum wave number of 1.8×10^{-3} cm^{-1}, Doppler shifts as large as 4500 Hz are possible. The spacecraft observed frequency spectrum can be produced by the ion-acoustic wave mode.
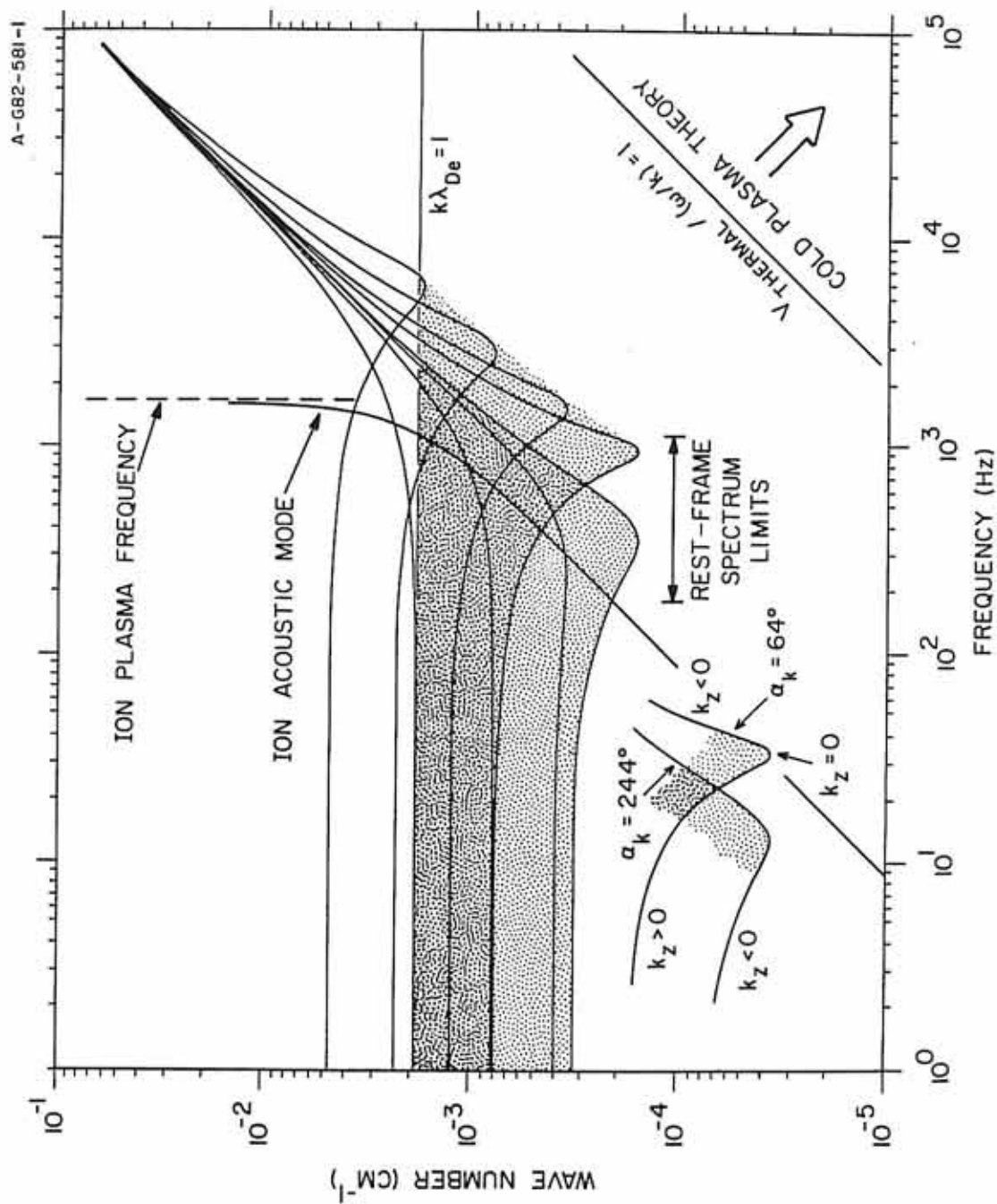
Figure 23

Figure 24   Ion-acoustic mode group velocity is graphed. Group
velocity is plotted vertically and frequency
horizontally. The dashed line indicates the bulk
plasma flow velocity. The limits for the rest-
frame frequency from Figure 23 are marked, showing
that the group velocities are at least a factor of
3 less than the plasma flow. Propagation of ion-
acoustic mode waves will be dominated by the bulk
plasma motion and be convected from locations up-
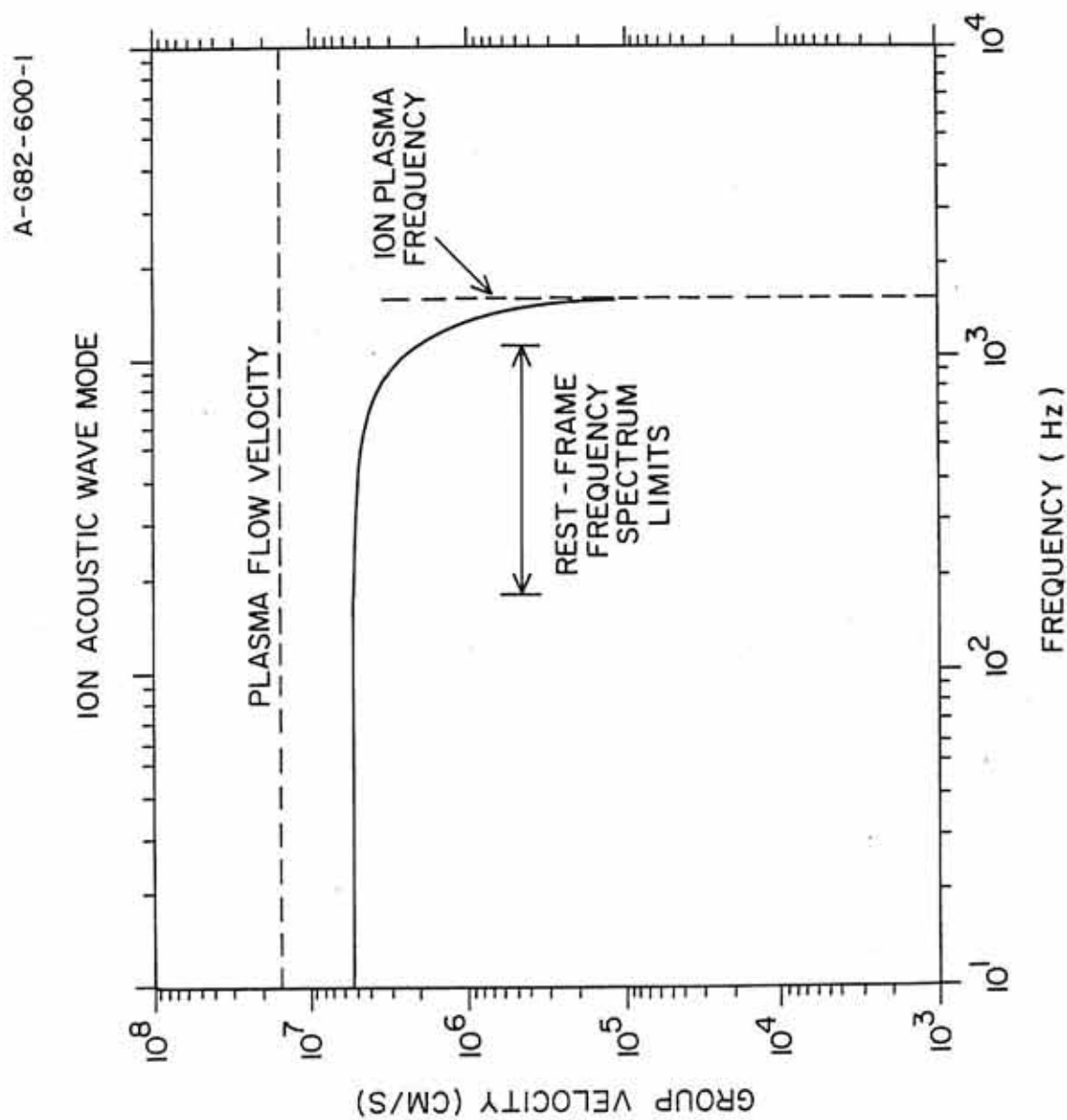stream of the spacecraft.

Figure 24